

# Assessment of the Quality of MODIS Cloud Products from Radiance Simulations

SEUNG-HEE HAM AND BYUNG-JU SOHN

*School of Earth and Environmental Sciences, Seoul National University, Seoul, South Korea*

PING YANG

*Department of Atmospheric Sciences, Texas A&M University, College Station, Texas*

BRYAN A. BAUM

*Space Science and Engineering Center, University of Wisconsin—Madison, Madison, Wisconsin*

(Manuscript received 22 September 2008, in final form 18 February 2009)

## ABSTRACT

Observations made by the Moderate Resolution Imaging Spectroradiometer (MODIS), the Atmospheric Infrared Sounder (AIRS), the *Cloud–Aerosol Lidar and Infrared Pathfinder Satellite Observation (CALIPSO)*, and *CloudSat* are synergistically used to evaluate the accuracy of theoretical simulations of the radiances at the top of the atmosphere (TOA). Specifically, TOA radiances of 15 MODIS bands are simulated for overcast, optically thick, and single-phase clouds only over the ocean from 60°N to 60°S, corresponding to about 12% of all the MODIS cloud observations. Plane parallel atmosphere is assumed in the simulation by restricting viewing/solar zenith angle to be less than 40°. Input data for the radiative transfer model (RTM) are obtained from the operational MODIS-retrieved cloud optical thickness, effective radius, and cloud-top pressure (converted to height) collocated with the AIRS-retrieved temperature and humidity profiles. In the RTM, ice cloud bulk scattering properties, based on theoretical scattering computations and in situ microphysical data, are used for the radiative transfer simulations. The results show that radiances for shortwave bands between 0.466 and 0.857  $\mu\text{m}$  appear to be very accurate with errors on the order of 5%, implying that MODIS cloud parameters provide sufficient information for the radiance simulations. However, simulated radiances for the 1.24-, 1.63-, and 3.78- $\mu\text{m}$  bands do not agree as well with the observed radiances as a result of the use of a single effective radius for a cloud layer that may be vertically inhomogeneous in reality. Furthermore, simulated radiances for the water vapor absorption bands located near 0.93 and 1.38  $\mu\text{m}$  show positive biases, whereas the window bands from 8.5 to 12  $\mu\text{m}$  show negative biases compared to observations, likely due to the less accurate estimate of cloud-top and cloud-base heights. It is further shown that the accuracies of the simulations for water vapor and window bands can be substantially improved by accounting for the vertical cloud distribution provided by the *CALIPSO* and *CloudSat* measurements.

## 1. Introduction

Clouds cover about 65%–70% of the globe on average and are regarded as the most important factors in modulating the earth radiation budget (ERB). There are two competing ways in which clouds influence the ERB, that is, the *cloud albedo effect* associated with the reflection of incoming solar radiation by clouds and the *greenhouse effect* associated with the trapping of

outgoing longwave radiation (OLR) by clouds (Liou 2002). The imbalance between those two effects determines the net cloud radiative forcing (CRF) that fundamentally influences weather and climate systems (e.g., Sohn and Smith 1992).

At present, various studies reported in the literature concur that clouds produce a global cooling effect on the ERB (Ramanathan et al. 1989; Hartmann and Doelling 1991; Solomon et al. 2007). However, the cloud cooling effect might be enhanced or weakened by changes in atmospheric conditions, because cloud coverage and type also change in response to climate perturbations and then CRF can be modified, which is known as *cloud feedback*. Substantial efforts have been made to understand cloud

---

*Corresponding author address:* Prof. Byung-Ju Sohn, School of Earth and Environmental Sciences, Seoul National University, NS 80, Seoul 151-747, South Korea.  
E-mail: sohn@snu.ac.kr

feedback mechanisms as a consequence of the increase of sea surface temperature (SST) or the increase of the amount of CO<sub>2</sub> in the atmosphere, but there are still significant uncertainties in current general circulation models (GCMs). The uncertainties are largely caused by inaccurate parameterizations or treatments of the formation, growth, optical properties, and vertical structure of clouds in the model simulations. Accurate measurements of cloud properties—such as cloud albedo, cloud optical thickness (COT), and effective particle radius—are thus crucial to understanding cloud–climate radiative interactions and to improving cloud schemes in GCMs.

Satellite sensors provide measurements that can be used to infer cloud properties globally. Broadband instruments such as Earth Radiation Budget Experiment (ERBE), Clouds and the Earth's Radiant Energy System (CERES), and Scanner for Radiation Budget (ScaRaB) directly observe top-of-atmosphere (TOA) radiances (Barkstrom and Smith 1986; Wielicki et al. 1996; Kandel et al. 1998). These radiances, in conjunction with angular distribution models, are converted to TOA fluxes that can be used subsequently to determine the CRF. On the other hand, narrowband instruments—such as the Advanced Very High Resolution Radiometer (AVHRR), Moderate Resolution Imaging Spectroradiometer (MODIS), and Spinning Enhanced Visible (VIS) Infrared (IR) Imager (SEVIRI)—provide more detailed information that can be used to infer cloud properties, including cloud-top pressure/temperature/height, cloud thermodynamic phase, optical thickness, and effective particle size (e.g., Platnick et al. 2003; Roebeling et al. 2006). Within a given atmospheric column, the vertical distribution of clouds is available from satellite-borne active sensors, such as *CloudSat* (Stephens et al. 2002) and *Cloud–Aerosol Lidar and Infrared Pathfinder Satellite Observations* (CALIPSO; Winker et al. 2003). From these observed cloud parameters, more realistic parameterization schemes can be developed for GCMs through which uncertainties in current climate models can be examined. However, significant errors in estimating the radiative forcing of clouds can be introduced by uncertainties in the satellite cloud products (Yang et al. 2007). Thus, it is important to assess the quality of cloud products inferred from satellite observations.

The current approach to passive remote sensing of clouds from narrowband observations (e.g., MODIS measurements) essentially employs a multispectral approach. This approach is based on the assumption that there are some wavelengths where scattering or absorption by cloud particles is dominant. Algorithms can be employed to infer a given cloud parameter that best

exploits the information content in the bands. For example, the correlation of two bands centered at visible and shortwave (SW)-infrared (SWIR) wavelengths can be used to retrieve COT and effective particle size simultaneously (Nakajima and King 1990). Bands located within the 15- $\mu\text{m}$  CO<sub>2</sub> band can be used to infer cloud-top pressure (CTP) for mid- to high-level clouds, whereas the IR window band (11  $\mu\text{m}$ ) can be used to infer low-level cloud-top temperature (CTT; Menzel et al. 2006, 2008; Platnick et al. 2003). Furthermore, because the imaginary parts of the refractive index of ice and water are different between 8.5 and 11  $\mu\text{m}$ , two IR window bands centered at 8.5 and 11  $\mu\text{m}$  can be used to differentiate the cloud thermodynamic phase (Platnick et al. 2003). Because the cloud parameters are inferred from different spectral bands, it is necessary to check the consistency between the retrieved products. There have been efforts to examine the consistency among the observed radiative parameters. For example, Smith et al. (2005) performed closure studies between measured aerosol optical properties and shortwave fluxes, and Turner et al. (2004) investigated the consistency between a water vapor absorption model and the IR spectrum observations.

In this study, MODIS pixel radiances are simulated for the 15 bands listed in Table 1 using state-of-the-art scattering and radiative transfer modeling capabilities. Subsequently, the simulated radiances will be compared with the observed radiances. These 15 bands are used in various MODIS algorithms to infer aerosol and cloud properties, such as in the MODIS cloud mask (Frey et al. 2008) and the IR cloud thermodynamic phase (bands 29 and 31). Seven of the 15 bands (MODIS bands 1, 2, 5, 6, 7, and 20) are used in the inference of COT and effective particle size. These bands are directly influenced by the presence of clouds. In addition, bands located at around 6–7  $\mu\text{m}$  (bands 27 and 28) and around 15  $\mu\text{m}$  (bands 33–36) are excluded because of strong water vapor and carbon dioxide bands. The present simulations provide an opportunity to examine the consistency between retrieved cloud products and measured radiances for the 15 bands subject to the errors in the radiative transfer simulations. Because noise and bias of MODIS measurements are negligible (Xiong and Barnes 2003; Tobin et al. 2006), the difference between observed and simulated radiances can be attributed to uncertainties in input variables and/or modeling deficiencies. In addition, ice cloud effective particle size inferred from different spectral bands based on the ice cloud bulk scattering properties (Baum et al. 2005a,b) can be used to assess the retrieved optical property data. Moreover, in this study the effects of cloud vertical profile are investigated using *CloudSat* and *CALIPSO* measurements.

TABLE 1. Characteristics of the 15 MODIS bands (1–7, 17–19, 26, 20, 29, 31, and 32; band 26 is set with the other water vapor bands) in this study and cloud products retrieved from the corresponding band.

Band	Center wavelength ( $\mu\text{m}$ )	Bandwidth ( $\mu\text{m}$ )	Primary absorber	Cloud products
1	0.646	0.043	Ozone, water vapor	COT over land
2	0.857	0.040		COT over ocean
3	0.466	0.018		
4	0.554	0.020	Ozone	
5	1.24	0.024	Cloud droplet	COT over snow
6	1.63	0.028	Cloud droplet	$r_e$
7	2.11	0.052	Cloud droplet	$r_e$
17	0.904	0.036	Water vapor	
18	0.936	0.014	Water vapor	
19	0.936	0.047	Water vapor	
26	1.38	0.038	Water vapor	Cloud phase
20	3.78	0.182	Water vapor, cloud droplet	$r_e$
29	8.55	0.382	Cloud droplet (strong absorption)	Cloud phase
31	11	0.530	Cloud droplet (strong absorption)	Cloud phase, CTP for low clouds
32	12	0.512	Cloud droplet (strong absorption)	Cloud phase

## 2. Methodology

### a. Data

#### 1) COLLOCATED DATASET BETWEEN MODIS, AIRS, *CLOUDSAT*, AND *CALIPSO*

In this study, the measurements by the *Aqua* MODIS (Salomonson et al. 1989; Barnes et al. 1998), Atmospheric Infrared Sounder (Aumann et al. 2003), *CloudSat* (Stephens et al. 2002), and *CALIPSO* (Winker et al. 2003) during January 2007 are collocated. Because *CloudSat* and *CALIPSO* essentially make measurements along their tracks, whereas MODIS and AIRS are cross-track scanners aboard *Aqua*, the collocation is carried out through the along-track observations made by the *CloudSat* track. For a given *CloudSat* pixel, the closest MODIS, AIRS, and *CALIPSO* pixels are chosen within  $0.1^\circ$ ,  $0.5^\circ$ , and  $0.1^\circ$  radii, respectively. The time difference for the collocation is not counted because the time difference is around 75 s between *Aqua* (MODIS/AIRS) and *CALIPSO* and less than 75 s between *Aqua* (MODIS/AIRS) and *CloudSat*.

MODIS-derived cloud parameters (MYD06) and AIRS atmospheric profile data [AIRS level 2 Standard Retrieval Product (AIRS2RET)] are used as inputs to a radiative transfer model (RTM) to simulate radiances for the 15 MODIS bands listed in Table 1. The simulated results are compared with observed MODIS radiances (MYD021) to assess the quality of MODIS cloud products. Note that AIRS profiles likely have a reduced quality in the presence of clouds as compared to the clear condition (Susskind et al. 2003). Therefore, quality indicators of “PBest/PGood” are used to remove the cases when the entire IR retrieval fails (Fishbein et al. 2007; Susskind et al. 2007). In addition, AIRS profile data

are used only if the tropopause pressure is inferred, which requires more than a single retrieval path (Fishbein et al. 2007), to ensure the quality of AIRS profile data.

*CloudSat* and *CALIPSO* data are used to examine the influences of multiple cloud layers and cloud boundaries on the simulation errors. *CloudSat* carries the Cloud Profiling Radar (CPR) that measures cloud vertical profiles at a frequency of 94 GHz. The *CloudSat* 2B-GEOPROF product provides cloud mask values from 0 to 40 for 125 height bins. A zero value means no cloud layer exists, whereas values from 20 to 40 indicate the presence of cloud for the given height. A value of 30 is chosen to provide a stable threshold value for the presence of clouds in a given layer (Mace et al. 2007). Thus, cloud-top and cloud-base heights are calculated at the boundary of the region where the cloud mask value is greater than 30. It has been noted that a radar beam can penetrate through thick clouds and is insensitive to small ice particles (Kahn et al. 2008). For this reason, cirrus clouds are often missed in *CloudSat* observations; therefore, *CALIPSO* data are used. *CALIPSO* carries the Cloud–Aerosol Lidar with Orthogonal Polarization (CALIOP), which observes backscattered signals at wavelengths 532 and 1064 nm. *CALIPSO* data provide information about the number of cloud layers and cloud-top/cloud-base heights. By combining *CloudSat* and *CALIPSO* data, more accurate information, including information about cirrus clouds, is obtained for multiple cloud layers.

#### 2) MODIS CLOUD PARAMETERS

In the MODIS cloud products, the retrieval of COT over land, ocean, and snow is based on information contents at 0.646, 0.857, and  $1.24 \mu\text{m}$  (bands 1, 2, and 5),

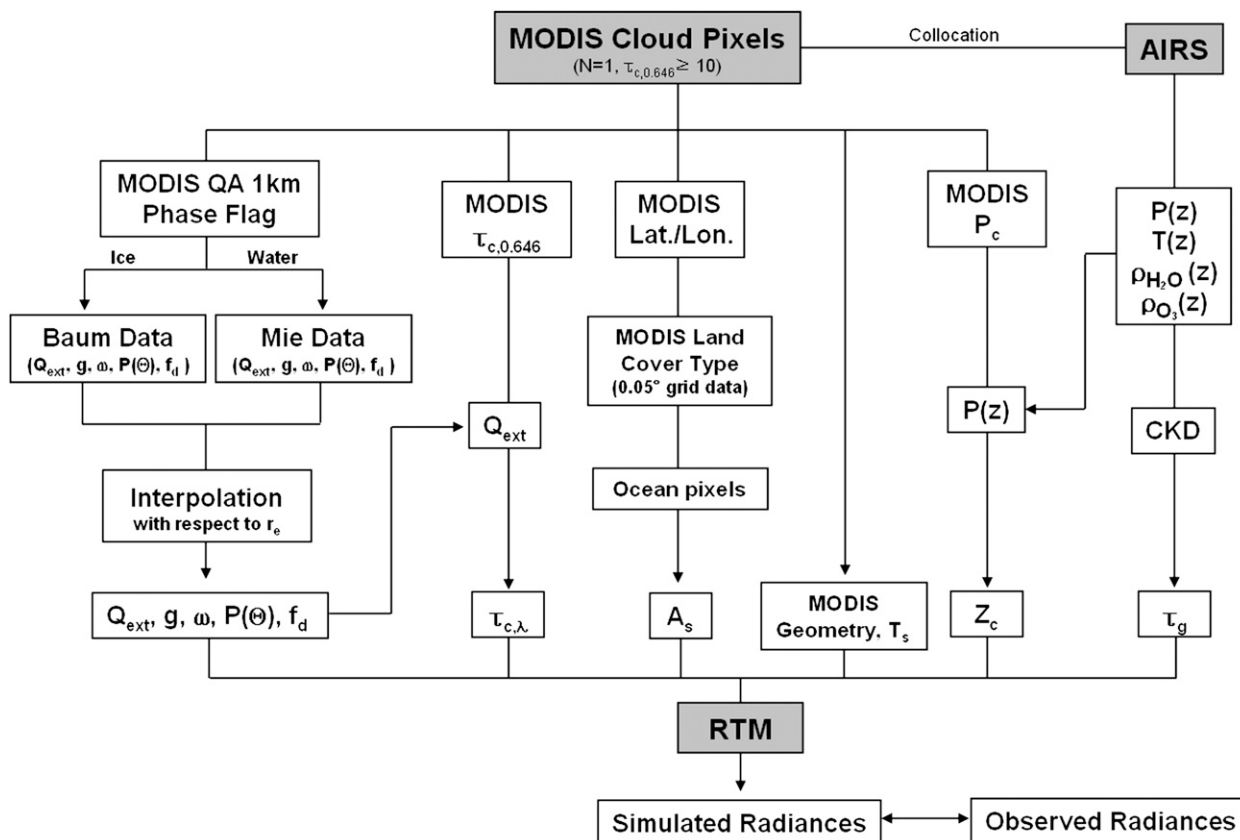


FIG. 1. A schematic diagram showing the simulation process for 15 MODIS bands using MODIS cloud products and AIRS atmospheric profiles.

respectively. Three bands at 1.63, 2.11, and 3.78  $\mu\text{m}$  (bands 6, 7, and 20) have relatively strong absorption by cloud particles and are used to estimate effective particle radius (King et al. 1997). The 1.63- and 2.11- $\mu\text{m}$  bands are referred to as SWIR bands, whereas the 3.7- $\mu\text{m}$  band is referred to as a near-infrared (NIR) band. Although particle sizes are inferred from the three SWIR/NIR bands, the MODIS product provides the result at 2.11  $\mu\text{m}$ . The ratios of the retrieved particle sizes from the 1.63- and 3.78- $\mu\text{m}$  bands to that from the 2.11- $\mu\text{m}$  band provide a quality check of the retrieval.

The  $\text{CO}_2$  slicing method for retrieving CTP is implemented with four MODIS bands at 13.3, 13.6, 13.9, and 14.2  $\mu\text{m}$  (Menzel et al. 2008). However, the  $\text{CO}_2$  slicing method is only used for clouds residing at pressures less than the approximately 700-hPa level because the signal-to-noise ratio becomes too small for low-level clouds. Low clouds are assumed to be opaque, and then CTT is inferred by comparing the measured 11- $\mu\text{m}$  brightness temperature with that derived from the atmospheric temperature and water vapor profile. The cloud-top height (CTH) and CTP are then inferred

based on the CTT and the atmospheric profiles. However, this assumption would likely cause an overestimation of CTP (Platnick et al. 2003) because much of low cloud is not opaque (Turner et al. 2007).

### 3) SCATTERING PROPERTY DATA

To specify cloud optical properties in the RTM, ice cloud bulk scattering properties are used following the methodology in Baum et al. (2005a,b). These are the same models used for the MODIS collection-5 version COT retrievals of ice clouds (King et al. 2006), whereas Mie scattering calculations are used for water clouds. The Baum scattering data were developed to incorporate nonspherical ice particle properties based on in situ measurements from a variety of midlatitude and tropical ice cloud field experiments (Heymsfield et al. 2002). From those observational results, particle size distributions (PSDs) and six habit fractions are defined in Baum et al. (2005a) and the single-scattering properties of nonspherical ice particles (Yang et al. 2003, 2005)—such as the extinction efficiency ( $Q_{\text{ext}}$ ), asymmetry factor ( $g$ ), phase function [ $P(\Theta)$ ], single-scattering albedo (SSA;  $\omega$ ),

and fraction of the delta-transmission ( $f_d$ )—are integrated over the PSDs to obtain averaged scattering properties (Baum et al. 2005b).

For water clouds, a Mie scattering code is used to simulate the optical properties of spherical liquid water droplets. The PSD,  $N(r)$ , of liquid water droplets is assumed to follow the gamma distribution, that is,

$$N(r) = \frac{(\alpha + 3)^{\alpha+1}}{\Gamma(\alpha + 1)} \frac{r^\alpha}{r_e^{\alpha+1}} \exp\left[-(\alpha + 3)\left(\frac{r}{r_e}\right)\right], \quad (1)$$

where  $r$ ,  $r_e$ , and  $\alpha$  are the radius, effective radius, and shape parameter, respectively. In this study, we use  $\alpha = 6$ , and  $5 \mu\text{m} \leq \text{effective radius } (r_e) \leq 90 \mu\text{m}$  with a  $5\text{-}\mu\text{m}$  interval (thus 18 size bins are considered).

### b. Input data to radiative transfer model

Cloud parameters and AIRS atmospheric profiles of temperature and water vapor mixing ratio are used for the RTM simulations once the targets are selected. A detailed flowchart of the simulation process is presented in Fig. 1. MODIS cloud pixels are selected if COT at  $0.646 \mu\text{m}$  is greater than 10 (i.e.  $\tau_{c,0.646} \geq 10$ ) to reduce the surface albedo influences on the TOA radiance simulation. A cloud fraction of 1 ( $N = 1$ ) is applied to exclude broken clouds. The MODIS quality assurance (QA) is used to filter out those pixels with unknown or mixed phase and to further classify each selected pixel as an ice cloudy or water cloudy pixel. It has been shown that misidentification of cloud phase can induce significant errors in cloud retrievals (e.g., Nasiri and Kahn 2008) and thus substantial errors in cloud radiance simulations. The Baum (2005a,b) and Mie scattering models are used for clouds that are determined to be either ice or water phase as determined from the QA flags, respectively. Because the Baum and Mie models provide averaged optical properties for 15 MODIS bands and for 18 effective size bins, the provided scattering parameters [ $Q_{\text{ext}}$ ,  $g$ ,  $\omega$ ,  $P(\Theta)$ , and  $f_d$ ] may be linearly interpolated to obtain appropriate properties for a given effective radius ( $r_e$ ). Because the MODIS cloud product only provides COT for the  $0.646\text{-}\mu\text{m}$  band ( $\tau_{c,0.646}$ ), the extinction efficiency is used to scale COT for other bands ( $\tau_{c,\lambda}$ ) as follows:

$$\tau_{c,\lambda} = \tau_{c,0.646} \frac{Q_{\text{ext},\lambda}}{Q_{\text{ext},0.646}}, \quad (2)$$

where  $Q_{\text{ext},0.646}$  represents an extinction efficiency at  $0.646\text{-}\mu\text{m}$  band obtained from the Baum and Mie models for ice and water clouds, respectively.

By taking MODIS land cover data into account, which is given in  $0.05^\circ$  grid format, only ocean pixels are kept

to minimize errors induced by surface reflectance ( $A_s$ ). A bidirectional reflectance distribution function (BRDF) model for the ocean is adopted from the Santa Barbara discrete ordinate radiative transfer (DISORT) Atmospheric Radiative Transfer (SBDART; Ricchiazzi et al. 1998) model to consider reflectance variations with viewing geometry. In addition, MODIS surface temperature ( $T_s$ ) data with a  $5\text{-km}$  resolution is used for the calculation of surface emission for IR bands. MODIS viewing geometries—such as solar zenith angle (SZA), solar azimuth angle (SAA), viewing zenith angle (VZA), and viewing azimuth angle (VAA)—are also included in the simulation of TOA satellite-level radiances.

To define a cloud layer in the radiative transfer simulations, CTP ( $P_c$ ) is converted into geometric height ( $Z_c$ ) in kilometers, using an AIRS pressure profile [ $P(z)$ ] with the assumption that the cloud depth ( $\Delta Z_c$ ) is  $1 \text{ km}$ . The assumption of the  $1\text{-km}$  depth is thought to be reasonable for the purpose of TOA radiance simulations because TOA radiances in the visible bands are dependent primarily on the total COT itself, and the  $1\text{-km}$  cloud layer can be treated as a blackbody. However, this assumption may significantly influence some of 15 bands, as shown in Hong et al. (2007), and this will be examined using detailed information of cloud vertical extent obtained from *CloudSat* and *CALIPSO* measurements.

Temperature [ $T(z)$ ], ozone [ $\rho_{\text{O}_3}(z)$ ], and water vapor profiles [ $\rho_{\text{H}_2\text{O}}(z)$ ] for 28 levels are also specified using AIRS profile data. Then the correlated- $k$  distribution (CKD) method is used to account for the gaseous absorption (Kratz 1995; Kratz and Rose 1999).

### c. Radiative transfer modeling for clouds

The DISORT (Stamnes et al. 1988) model, implemented with 32 streams, is used for the simulation of the radiances at 15 MODIS bands. However, 32 streams may not be sufficient for cloud radiative transfer modeling because the phase function associated with large cloud particles has a strong forward peak, which may mean that thousands of Legendre terms are required to accurately account for the full scattering phase function (King 1983; Nakajima and Tanaka 1988; Hu et al. 2000). Therefore, delta-transmission and diffraction peaks of the phase function are truncated; details may be found in Wiscombe (1977), Yang et al. (2000), and references therein.

The Baum (2005b) and Mie phase functions show different features, resulting in different angular distributions of reflectance despite similar flux reflectance values. Figure 2 shows the cloud bidirectional reflectance factors (BRFs) at  $0.646 \mu\text{m}$  for ice and water phase clouds when  $\text{COT} = 40$ ,  $\text{SZA} = 30^\circ$ , and  $10 \mu\text{m} \leq r_e \leq 60 \mu\text{m}$ . The radial axis represents the VZA ( $\theta_v$ ), and the tangential axis represents the relative azimuth



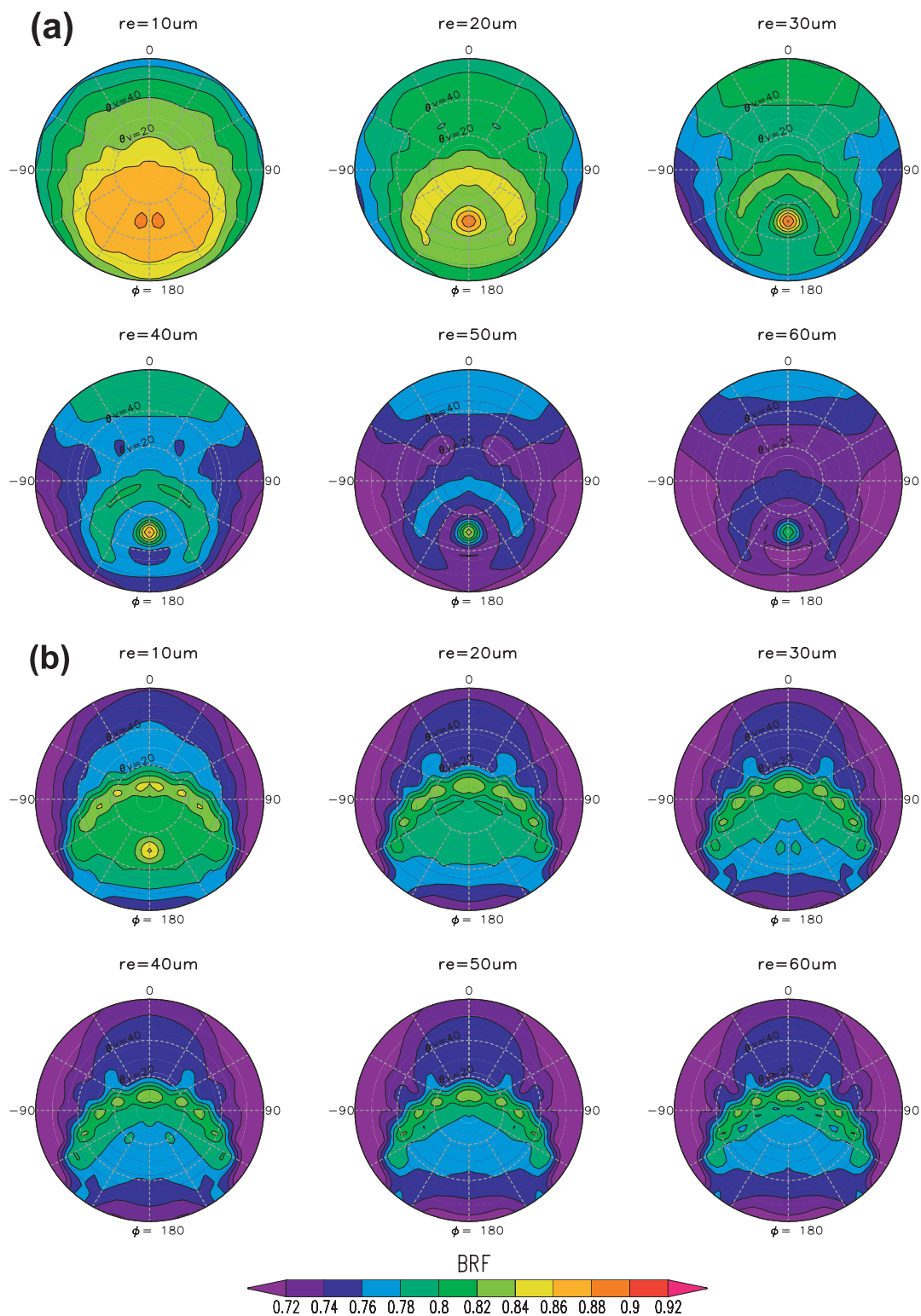


FIG. 2. Simulated cloud BRF at  $0.646\text{-}\mu\text{m}$  band using (a) Baum and (b) Mie phase functions, when  $\text{COT} = 40$  and  $\text{SZA} = 30$ . Radial axis and tangential axis mean VZA and RAA, respectively.

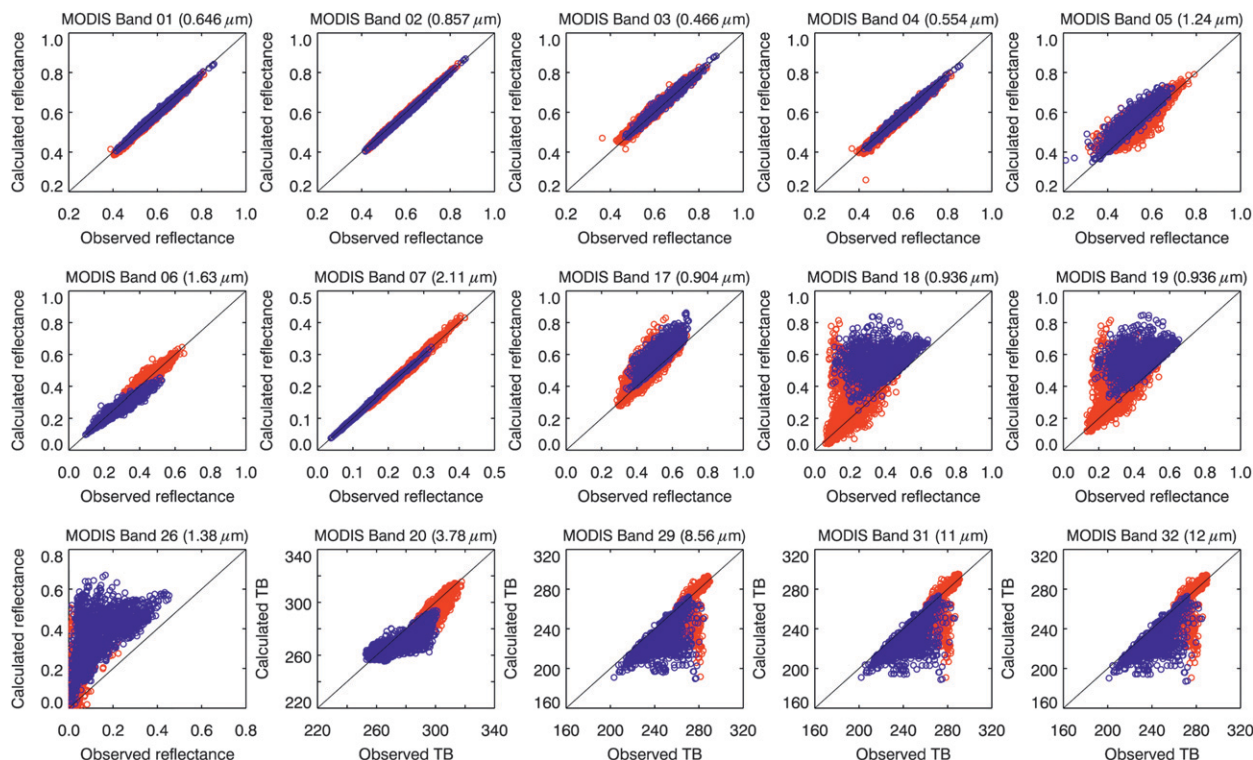


FIG. 3. Scatterplots of simulated vs observed reflectances (or TBs) at 15 MODIS bands for ice (blue circles) and water (red circles) cloud pixels. Simulations produced using AIRS profiles and MODIS cloud products as inputs to the RTM.

angle (RAA;  $\varphi$ ). The RAA is defined as  $0^\circ$  if forward propagation occurs, whereas backward propagation of sunlight is  $180^\circ$ . Maximum reflectance occurs when  $\text{RAA} = 180^\circ$  and  $\text{VZA} = 30^\circ$  for the ice cloud case manifesting the dominant backward reflection. Water cloud BRFs also show maxima around the backscattering angles but with slightly different features from those found in the case for ice clouds. The differences in cloud BRFs between ice and water clouds imply that misidentification of the cloud phase can cause significant error in estimating the COT and effective radius. Furthermore, it can be shown that both BRFs vary from 0.7 to 0.9 if  $\text{VZA} \leq 60^\circ$ , suggesting that the cloud layer cannot be treated as a Lambertian surface because cloud reflectance is strongly affected by viewing and solar geometries. Figure 2 also shows the dependence of BRFs on  $r_e$ . In both ice and water clouds, as  $r_e$  increases, the asymmetry factor increases and the SSA decreases, resulting in a decrease in BRFs.

### 3. Results

#### a. Simulation results

Radiances are simulated for 15 MODIS bands for selected MODIS cloud pixels using AIRS profiles and MODIS cloud parameters as inputs to the DISORT

RTM. Comparisons of reflectances (for VIS/SWIR bands) or brightness temperatures (TBs from NIR/IR bands) are made between the calculated and observed values, with some results given in Fig. 3.

It is noted that SW bands from 0.466 to  $0.857 \mu\text{m}$  (bands 1–4) can be simulated within about a 5% uncertainty range regardless of cloud phase when cloud conditions are described using MODIS cloud products. Considering that COTs at bands 2–4 are obtained by scaling extinction efficiencies between two bands of interest, as in Eq. (2), the close agreement shown in Fig. 3 suggests that the scattering property data used in this study are reasonably accurate. However, more examination may be needed for the SWIR/NIR/IR bands because the size parameters for the visible spectral regions with cloud particles tend to be large, and thus the extinction efficiency used for the scaling is unlikely to vary with the wavelength.

As expected, simulated reflectances for band 2 ( $0.857 \mu\text{m}$ ) and band 7 ( $2.11 \mu\text{m}$ ) are in good agreement with observed values, probably because those bands are used for the retrieval of COT and effective radius, respectively. Note that only ocean pixels are considered in this simulation, and COTs over the ocean are retrieved from  $0.857\text{-}\mu\text{m}$  band measurements. This explains the better agreement of the  $0.857\text{-}\mu\text{m}$  band reflectances in comparison to the  $0.646\text{-}\mu\text{m}$  band, which is used for the

retrieval of COT over land. The same explanation can be applied to the 1.24- $\mu\text{m}$  band that is used for the COT retrieval over the snow, but with a more scattered pattern.

Bands 5–7 and 20 (1.24, 1.63, 2.11, and 3.78  $\mu\text{m}$ ) represent SWIR/NIR bands showing relatively strong cloud absorption. Among those four bands, the largest imaginary part of refractive index occurs at 3.78  $\mu\text{m}$ , implying that the strongest absorption by cloud particles occurs in this band. The band at 1.24  $\mu\text{m}$  shows the weakest absorption, whereas 1.63 and 2.11  $\mu\text{m}$  show absorption in between (Ackerman and Stephens 1987; Palmer and Williams 1974). As a result, the 3.78- $\mu\text{m}$  band is primarily sensitive to the cloud particles in the uppermost part of the cloud layer, whereas the 1.63-, 2.11-, and 1.24- $\mu\text{m}$  bands contain information about the absorption of solar radiation by cloud particles in deeper portions of the cloud layer (Platnick 2001).

The MODIS effective radius is inferred from band 7 (2.11  $\mu\text{m}$ ), which means that the retrieved effective radius is representative of the top-to-middle part of the cloud. Because the other SWIR/NIR bands represent different layers in the cloud, the more scattered distributions for bands 5, 6, and 20 in Fig. 3 may be due to the inhomogeneous vertical distribution of particle sizes. For example, if the updraft velocity is very low, then particle size sorting occurs; therefore, the smallest ice crystals are found in the uppermost layer, whereas larger particles are in the middle and bottom layers (Heymsfield and Iaquinta 2000). Scattered patterns showing a general overestimation of simulated 1.24- $\mu\text{m}$  band reflectances for ice cloud pixels (marked as blue circles) in Fig. 3 may be due to the use of 2.11- $\mu\text{m}$ -retrieved effective radii in the simulation, which could be smaller than 1.24- $\mu\text{m}$ -retrieved effective radii (SWIR reflectance increases as effective radius decreases). Likewise, scattered patterns toward the underestimation of simulated 3.78- $\mu\text{m}$  band TBs for ice cloud pixels in Fig. 3 could be related to the possibility that the 2.11- $\mu\text{m}$ -derived effective radii could be larger than the 3.78- $\mu\text{m}$ -derived effective radii. Therefore, it is expected that if we use effective radii derived from either a 1.63- or 3.78- $\mu\text{m}$  band as RTM inputs for the simulation of corresponding band, then simulated reflectances would show better agreements with the observed values. This assumption is investigated in more detail in appendix A.

Simulated reflectances at bands 17–19, and 26 (0.904, 0.936, 0.936, and 1.38  $\mu\text{m}$ ) in the water vapor absorption spectra centered at 0.93 and 1.38  $\mu\text{m}$  appear to be largely overestimated in comparison to the observed reflectances. For these water vapor bands, reflectances of low-level water clouds are much smaller than those of high-level ice clouds because of the tendency to have increased water vapor absorption near the surface. The

degree of overestimation of simulated reflectances appears to be proportional to the absorptivity of the water vapor band, suggesting that errors are closely related to uncertainties of cloud altitude, which determines the amount of water vapor absorption above and within the cloud layer. For example, differences in simulated reflectances at band 26 (1.38  $\mu\text{m}$ ) from the observed values are much larger compared to the results of bands 17–19 (0.904–0.936  $\mu\text{m}$ ). The larger differences probably occur because the water vapor absorption in the 1.38- $\mu\text{m}$  band is stronger than in the 0.904–0.936- $\mu\text{m}$  bands. In the same 0.93- $\mu\text{m}$  water vapor absorption band, band 18 (0.936  $\mu\text{m}$ ) has a more uncertain scattered pattern compared with band 17 (0.904  $\mu\text{m}$ ) for a similar reason—that is, band 18 is closer to the strong absorption line center. Comparison of band 18 with band 19 shows that simulations of the narrower band 18 are more uncertain than the wide band 19, implying that band 19 is less influenced by water vapor absorption because of the wider spectral coverage over the 0.93- $\mu\text{m}$  absorption band. A more detailed discussion on the overestimate related to the water vapor absorption band is provided in the next section with Fig. 4.

It is interesting to note that the IR window bands 29, 31, and 32 (8.56, 11, and 12  $\mu\text{m}$ ) show a general underestimation of simulated TBs. There seems to be two different groups in the scattered patterns—that is, one group (TB < 273 K in calculated TBs) shows a much larger underestimate with a highly scattered pattern for what are likely ice clouds and another group (TB > 273 K) shows a much smaller bias as well as less scattering and are likely to be water clouds. Consider that the CO<sub>2</sub> slicing method is applicable to clouds that reside above the approximately 700-hPa level (Menzel et al. 2008) and thus is unlikely to be used for low-level water clouds. Therefore, it seems that the different groups may be the result of the different retrieval methods of defining CTH. Because cloud heights retrieved directly from the 11- $\mu\text{m}$  band TB were used for the simulation of the 11- $\mu\text{m}$  band, the better agreement in the case of TB > 273 K does not necessarily mean more accurate CTH information.

#### *b. Detailed examination of water vapor and IR window bands*

To determine the error source associated with the simulations of radiances at water vapor and IR window bands, we examine in more detail the relationships between errors noted in those bands. In this analysis, simulation errors are defined by the differences between simulated and observed reflectances, or TBs. The relationships of band 17 (0.904  $\mu\text{m}$ ) versus band 19 (0.936  $\mu\text{m}$ ), band 19 (0.936  $\mu\text{m}$ ) versus band 26 (1.38  $\mu\text{m}$ ), and band 19 (0.936  $\mu\text{m}$ ) versus band 31 (11  $\mu\text{m}$ ) are



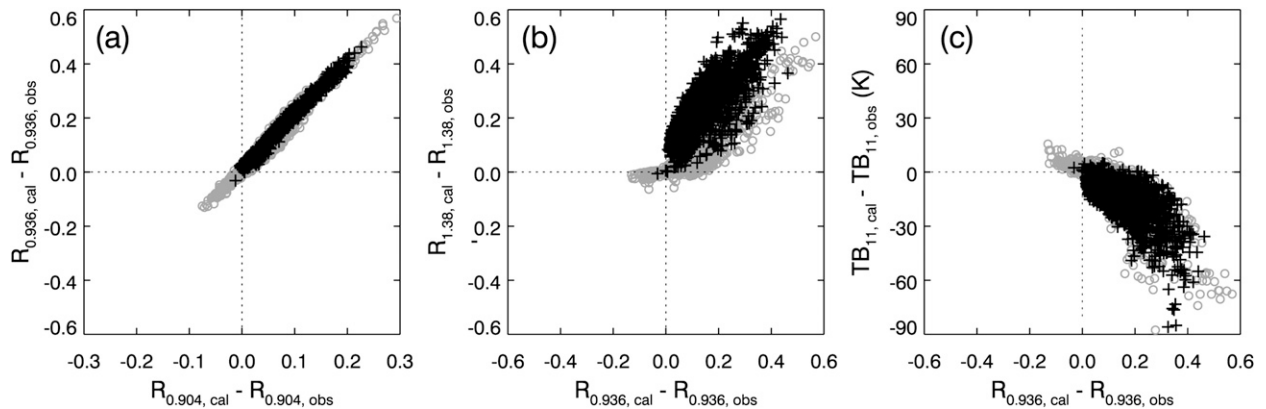


FIG. 4. Relationship of simulation errors between (a) band 17 ( $0.904 \mu\text{m}$ ) and band 19 ( $0.936 \mu\text{m}$ ) (b) band 19 ( $0.936 \mu\text{m}$ ) and band 26 ( $1.38 \mu\text{m}$ ) (c) band 19 ( $0.936 \mu\text{m}$ ) and band 31 ( $11 \mu\text{m}$ ) for ice (black crosses) and water (gray circles) cloud pixels. Simulation errors are defined as calculated minus observed.

given in Fig. 4. It is noted that both the  $0.904$ - and  $0.936$ - $\mu\text{m}$  bands, which are located in the same water vapor absorption band but at slightly different spectral positions, show positive errors as a result of the overestimation of reflectances when compared to the observed values. Although the errors for band 19 are about twice those for band 17, the errors appear to be linearly correlated because those two bands are located in the same water vapor absorption band. In comparison to band 17 versus band 19, the plot of simulation errors for band 19 versus band 26 shows a more scattered pattern despite the similar error range, most likely due to the different absorption spectra and channel response functions; the bandwidth of band 26 is narrower than band 19, and moreover, band 26 is located over a slightly more absorbing band. By comparison, band 31 shows negative simulation errors due to the underestimation of TBs, and those errors have opposite tendencies to the simulation errors found in water vapor bands (band 19), as evident from Fig. 4c.

We interpret the magnitude of simulation errors, degree of scattering, and correlation shown in Fig. 4 to be closely associated with the CTH and geometrical depth ( $\Delta Z_c$ ) of the cloud. If the retrieved CTH is higher than the true CTH, then water vapor absorption above the cloud becomes generally smaller. Thus simulated water vapor band reflectances would be greater than observed values because of the smaller water vapor absorption. Those effects for low clouds would be dependent upon the strength of the water vapor absorption at the spectral band of interest. For the  $1.38$ - $\mu\text{m}$  band, the influence of CTH error may be insignificant because the dominant column water vapor absorption above the cloud can mask the cloud-top contribution to the TOA radiance, as shown by the bundle of water pixels near 0 in Fig. 4b. In contrast, for bands showing relatively weak

water vapor absorption, such as bands 17–19, the influence of CTH errors on the TOA radiances becomes significant, even for the case of low clouds. More detailed results of the sensitivity of TOA radiance simulation to CTH errors are found in the appendix B.

Similar errors may be induced by multilayered clouds, in particular when thin cirrus clouds are overlaying a low-level water cloud. In such cases, the MODIS  $\text{CO}_2$  slicing method is highly sensitive to the presence of cirrus (Baum and Wielicki 1994; Kahn et al. 2007) because the  $\text{CO}_2$  bands have weighting functions that peak higher in the troposphere. Additionally, the  $\text{CO}_2$  slicing algorithm assumes that there is only one cloud layer in an atmospheric column, which is necessary for operational processing. As a result, the MODIS CTP algorithm tends to retrieve cloud pressures between the upper and lower cloud layers if there are multiple cloud layers, but it tends to be weighted toward the upper-level cloud (Weisz et al. 2007). If we use MODIS CTP for the model simulations, then simulated window band TBs are much colder than observed values because TOA radiances in the window bands may be dominated by optically thick low-level clouds even if optically thin ice clouds also reside in the column. Moreover, because most of the reflected signal from low cloud can be absorbed by water vapor in the strong water vapor absorption bands, underestimated CTP used in the model simulations should bring about overestimated reflectances in the water vapor bands (bands 17–19, and 26) as shown in Fig. 3. This interpretation will be examined further in the next section with the use of cloud layer information obtained from *CloudSat* and *CALIPSO*.

In the initial model simulation, cloud depth ( $\Delta Z_c$ ) is assumed to be 1 km. If the actual cloud depth is greater than 1 km, errors may be introduced that are similar to those induced by an incorrect CTH assignment mentioned

earlier. The smaller  $\Delta Z_c$  means a higher cloud base, implying a colder mean temperature of the cloud layer, which can result in smaller simulated TBs for the window bands in comparison to observed TBs. The smaller  $\Delta Z_c$  also implies less water vapor absorption of scattered light in the cloud layer, resulting in larger water vapor band reflectances compared to observations. This effect is also examined in detail in appendix B.

### c. Impact of the multilayered clouds on the radiance simulation

To investigate the influences of multilayered clouds on the simulation errors, in particular those noted in water vapor and window bands, we first classify used MODIS-AIRS-CloudSat-CALIPSO collocated pixels into pixels with single-layer clouds and pixels with multilayered clouds. The macrophysical information about the clouds in an atmospheric column—such as cloud top, cloud base, and multiple layers—is obtained from combining CloudSat and CALIPSO data. The classified single- and multilayered cloud cases are given in Figs. 5a and 5b, respectively. In Fig. 5, results for SW bands from 0.46 to 0.86  $\mu\text{m}$  (bands 1–4) and SWIR bands from 1.63 to 2.11  $\mu\text{m}$  (bands 5–7) are not shown because those bands are turned out to be not as influenced by the vertical distribution of cloud layers, as explained by the sensitivity tests in appendix B—that is, cloud altitude has negligible effects on VIS/SWIR bands. For the case of band 20 (3.78  $\mu\text{m}$ ), even though the band is sensitive to cloud-top and cloud-base heights due to emission components, Fig. 5 shows that there is not much difference between single and multiple layers. From the earlier interpretation, we conclude that the disagreement between observed and simulated reflectances for the SWIR/NIR bands (1.24, 1.63, and 3.78  $\mu\text{m}$ ) in Fig. 3 appears not because of cloud vertical structures but mainly as the result of the vertically inhomogeneous effective radius.

Except for band 20 (3.78  $\mu\text{m}$ ), far larger uncertainties of the model simulations are found in multilayered cloud cases, although single-layer cloud cases also show substantial biases and errors—in particular, for the water vapor bands, as shown in Fig. 5. From the results of sensitivity tests of CTH and  $\Delta Z_c$  in the appendix B, it is shown that IR window bands are more sensitive to CTH than  $\Delta Z_c$  when the COT becomes larger, because of the transmittance approaching zero. However, water vapor bands are sensitive to both CTH and  $\Delta Z_c$  because of water vapor absorption occurring in and above the cloud layer. Therefore, the relatively larger errors found in water vapor bands (top, Fig. 5a) compared to the IR bands (bottom, Fig. 5a) strongly suggest that simulation errors are largely because of misrepresented  $\Delta Z_c$  rather

than errors in MODIS-retrieved CTP/CTH in the single-layer cloud cases.

Multilayered cloud cases show more serious errors in simulating radiances for the water vapor and window bands. The errors occur because the MODIS retrieval algorithm causes large uncertainties in CTP/CTH for multilayered clouds—that is, the CO<sub>2</sub> slicing method used in the MODIS algorithm tends to retrieve CTP for the uppermost cloud layer. Optically thin upper-level cirrus may be the main problem in this case. The optical thickness of upper-level cirrus clouds is generally much smaller than the optical thickness of low-level water cloud, and thus TOA radiances are predominantly influenced by the low-level water cloud. It is clear that the uncertainties in MODIS CTP/CTH for multilayered cloud cases produce significant errors in water vapor and IR bands. This interpretation is further supported by the sensitivity test given in appendix B, that is, the COT rationing effects for two-layered cloud on reflectance (or TB). If a contribution of upper-layer COT to the total COT is less than 0.1, which is similar to the case of cirrus over thick water cloud, reflectances for the water vapor bands are mainly determined by lower cloud. On the other hand, TBs for the IR bands tend to have values between CTTs of lower and upper cloud, different from the COT contribution.

### d. Improvement of radiance simulations using CloudSat data

As discussed in the previous section, the correct specification of cloud top and cloud base is an important step in yielding accurate radiances for water vapor and IR window bands. Thus, it is assumed that radiance simulations for the 15 MODIS bands can be improved when accurate vertical-layer information is prescribed. We test this assumption using the vertical cloud information obtained from CloudSat data. In this test, for the single-layer cloud, a vertically homogeneous cloud is assumed between the cloud top and the cloud base. For the multilayered clouds, contributions to the COT by multiple cloud layers are assumed to be proportional to their respective depths. Note that the CALIPSO data are not used to allocate cloud layers because the CALIPSO lidar is much more sensitive to optically thin cirrus clouds than CloudSat. Thus the CALIPSO lidar detects a much deeper cirrus layer, causing erroneously large cirrus optical thickness when homogeneous cloud layers are considered. However, CloudSat and CALIPSO combined information is still used for classifying cloud pixels into pixels showing single and multiple layers.

In single-layer cloud cases, the correct specification of cloud depth based on the CloudSat data results in an improved radiance simulation for the water vapor bands

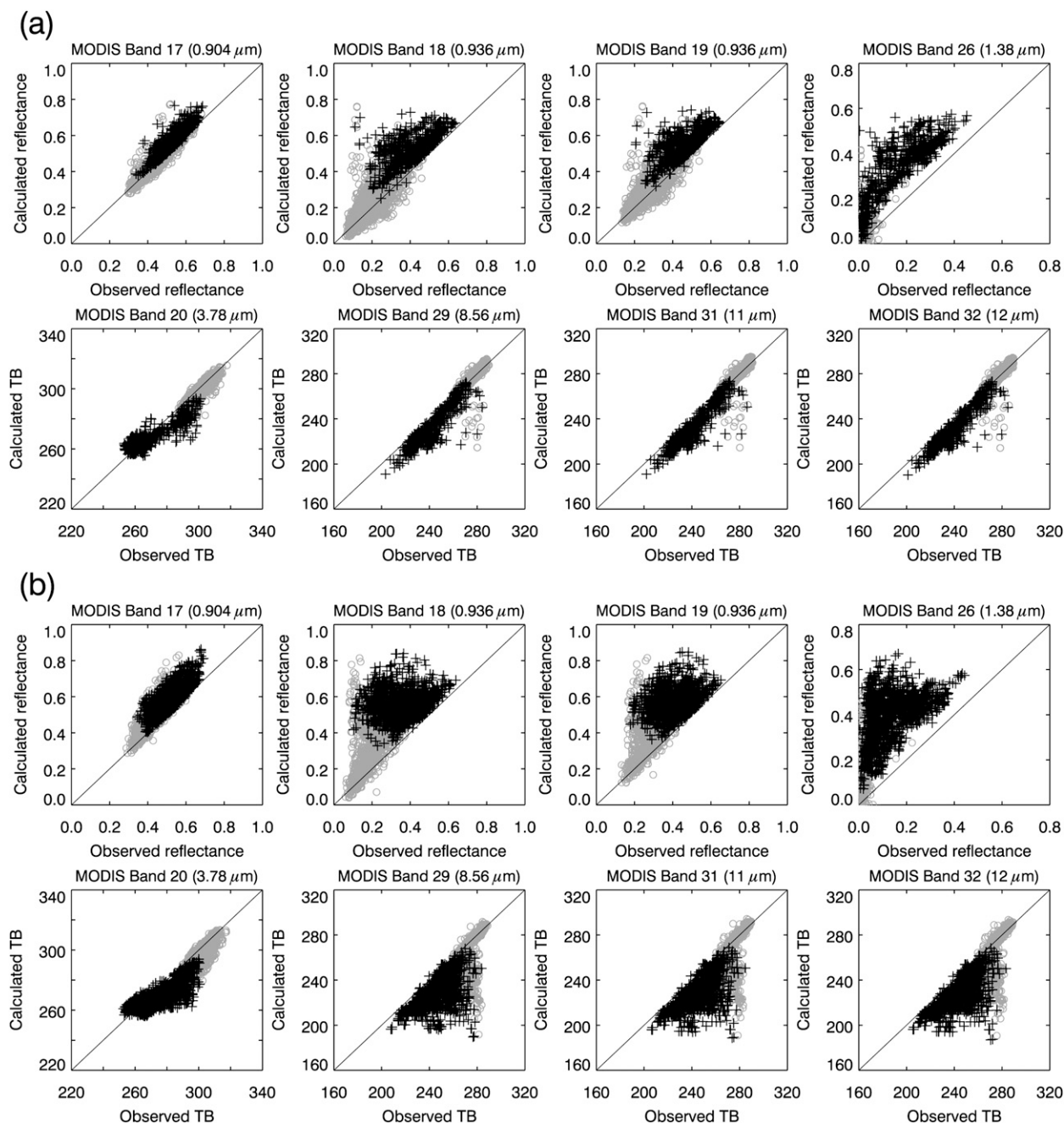


FIG. 5. Scatterplots of simulated vs observed reflectances (or TBs) at MODIS water vapor and window bands for ice (black crosses) and water (gray circles) cloud pixels. Simulations produced using AIRS profiles and MODIS cloud products (including CTP) for (a) single-layer clouds (b) multilayered clouds.

(top, Fig. 6a). In particular, 1.38- $\mu\text{m}$  band reflectances show significantly improved simulation results. In the sensitivity test, it was concluded that errors in water vapor band simulations are largely induced by the uncertain  $\Delta Z_c$  information. Improved results using *CloudSat*-derived  $\Delta Z_c$  information prove again the importance of the correct specification of cloud depth for an accurate

band simulation. In contrast, simulated window band TBs (bottom, Fig. 6a) show a scattering pattern not very different from simulation results without *CloudSat* information. Negative biases are still noted in simulated TBs, probably caused by vertically homogeneous optical properties assumed for the radiative transfer simulation. If water or ice particles were abundant in the

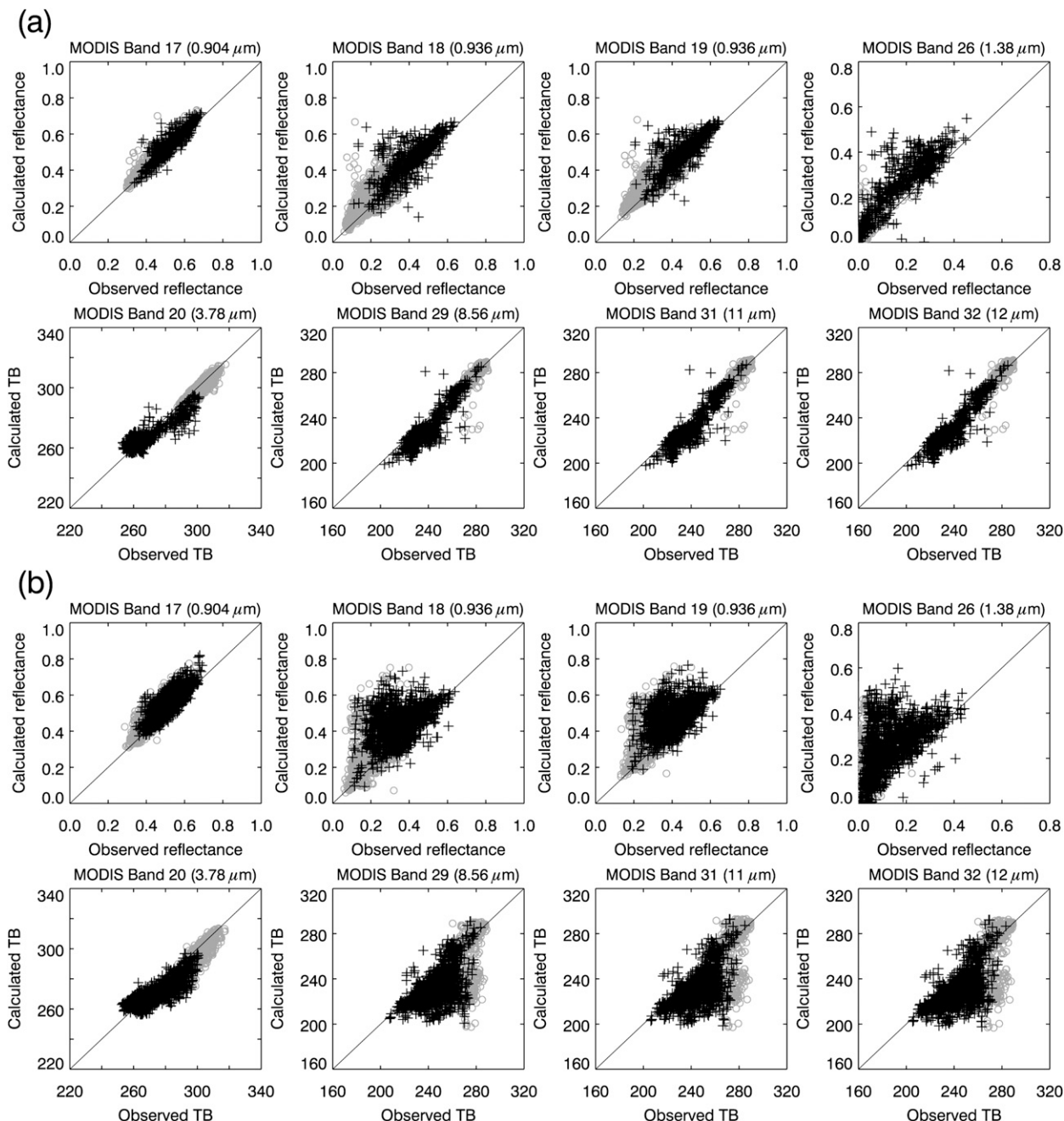


FIG. 6. As in Fig. 5 but for cloud-top and cloud-base heights specified from *CloudSat* data instead of MODIS CTP.

lower part of the cloud layer, then the cloud would emit more radiation than the homogeneous cloud. By the same reasoning, the water vapor bands show positive biases even though the use of *CloudSat* data greatly improved the simulation results.

In multilayered cloud cases, uncertainties in the simulated water vapor and window bands are reduced (Fig. 6b) compared to the cases using MODIS CTPs only (Fig. 5b). However, there still exist significant errors.

The relatively large uncertainties compared to single-layer cases may be not only the result of the incorrect specification of the cloud-top and cloud-base heights but also the result of the unrealistic specification of hydrometeor profiles. For example, in the case of thin cirrus lying above a thick altocumulus layer, the assumption of a homogeneous contribution to COT proportional to cloud depth would not be realistic because the primary contribution to COT is from the lower-level cloud,



although the COT rationing should also contribute to the scattering, as shown in appendix B.

Moreover, *CloudSat* often cannot detect very thin cirrus clouds. In the case when *CloudSat* misses, but *CALIPSO* detects, the optically thin cirrus cloud, the pixel is classified as a multilayered cloud in this study. However, only the single-layer information obtained from *CloudSat* data is used to specify cloud-top/cloud-base altitude, although the combination of *CloudSat* with *CALIPSO* data suggests the presence of a multilayer cloud. This could introduce a slight overestimation of IR window bands, as shown in the bundle of water pixels located in the diagonal of the lower panels of Fig. 6b.

#### 4. Summary and conclusions

The TOA radiances for 15 MODIS bands are simulated for cloud pixels collocated with AIRS, *CloudSat*, and *CALIPSO* measurements. In the simulation, only overcast (cloud fraction = 1), optically thick ( $\text{COT} \geq 10$ ), and single-phase clouds (ice or water) over ocean are used to minimize simulation errors caused by the characterization of the atmosphere, the surface, and the potential misidentification of the cloud thermodynamic phase. In addition, pixels having SZA and VZA less than  $40^\circ$  are chosen to reduce three-dimensional effects of the radiation. As a result, about 12% of all the MODIS cloud pixels are used in this study. For the simulations, the MODIS cloud products are used as input to a RTM, along with AIRS-retrieved atmospheric profiles. Bulk scattering models for ice clouds (Baum et al. 2005a,b) were used to take optical properties of nonspherical ice particles into account, whereas Mie scattering models were used for spherical water particles. The geometrical cloud depth was set to 1 km for the initial simulations.

The findings of this study are summarized as follows:

- Radiances for the SW bands between 0.466 and  $0.857 \mu\text{m}$  can be simulated within about a 5% uncertainty range, suggesting that the ice and water bulk scattering property models used in this study may provide reasonably accurate extinction efficiencies; these models were used for the COT scaling for the given band from MODIS COT at the  $0.646\text{-}\mu\text{m}$  band.
- Among the 15 bands, simulated radiances at  $0.857\text{-}$  and  $2.11\text{-}\mu\text{m}$  bands show the best agreement with observed values because those two bands were used for the retrieval of MODIS COT and effective particle size.
- Quite large deviations of the simulations from the observations were found for the  $1.24\text{-}$ ,  $1.63\text{-}$ , and  $3.78\text{-}\mu\text{m}$  SWIR/NIR bands, indicating that there may be some inconsistencies caused by an inhomogeneous vertical distribution of particle size in the cloud layer. Better

agreement between simulated and observed radiances is achieved for the  $1.63\text{-}$  and  $3.78\text{-}\mu\text{m}$  bands when those bands are simulated with effective radii retrieved from their respective band measurements.

- Simulated radiances in the water vapor and window bands show positive and negative biases, respectively, in comparison with MODIS measurements. The biases are thought to be due to less accurate CTP/CTH retrievals by MODIS for multilayered clouds and/or inaccurate cloud-base assignment. Note that MODIS does not infer cloud-base height, so a cloud geometrical depth was assumed in this study. This interpretation has been confirmed quantitatively from sensitivity tests with varying CTH and cloud geometrical depth ( $\Delta Z_c$ ).
- Multilayered cloud cases show much larger uncertainties in simulations due to errors in CTP/CTH and vertical depth of cloud layer associated with the MODIS products when multilayered clouds are present. The information about the vertical distribution of clouds, obtained from active measurements by *CloudSat* and *CALIPSO*, has proven to be very helpful for accurate water vapor and window band simulations.

Findings from the use of cloud-top and cloud-base height information from *CloudSat* are as follows:

- For single-layer cloud cases, simulations for the water vapor bands are improved because accurate cloud layer depth is used for the simulation. In contrast, window bands seem to be less affected by changes in cloud layer depth, because window band radiances are more sensitive to CTP/CTH than cloud layer depth for high values of COT.
- For multilayered cloud cases, uncertainties in water vapor and window bands appear to be reduced. However, significant errors associated with the vertical distribution of liquid/ice water content (LWC/IWC) still remain because the vertically homogeneous assumption results in large uncertainties despite the accurate specification of vertical shape and depth.

Overall, MODIS COT and effective radii seem to provide sufficient information for the radiance simulations at SW bands. However, for more accurate simulations in the SWIR/NIR bands, a single value of effective radius does not appear to be sufficient. Thus effective radii representing values at different layers may be needed. For the water vapor and window band simulations, MODIS cloud-top height information appears insufficient—particularly for the multilayered clouds that require the vertical distribution of LWC/IWC and

more correct cloud-top and cloud-base information. Those implications conversely suggest that the retrieval of effective radii for different layers (or vertical profiles of effective radii) may be possible by optimizing all VIS/SWIR/NIR bands whose sensitivity to cloud optical depth and effective radius depends on the cloud vertical profiles. By the same token, water vapor and window IR bands may be used for the improvement of the vertical structure of clouds, particularly when combined with the retrieved cloud optical parameters.

**Acknowledgments.** The authors thank two anonymous reviewers for their constructive and valuable comments, which led to an improved version of the manuscript. This work was supported by the National Space Lab program through the Korea Science and

Engineering Foundation, funded by the Ministry of Education, Science, and Technology (S10801000184-08A0100-18410) and by the BK21 Project of the Korean government. Support for Ping Yang is provided through NASA Grant NNX08AF68G and NSF Grant ATM-0239605. Support for Bryan Baum is provided through NASA Grant NNX08AF78A.

## APPENDIX A

### Influences of Effective Radius on the Simulation of TOA Radiances at SWIR/NIR Bands

The simulated reflectances at  $2.11\ \mu\text{m}$  show the best agreement with observed reflectances among the four

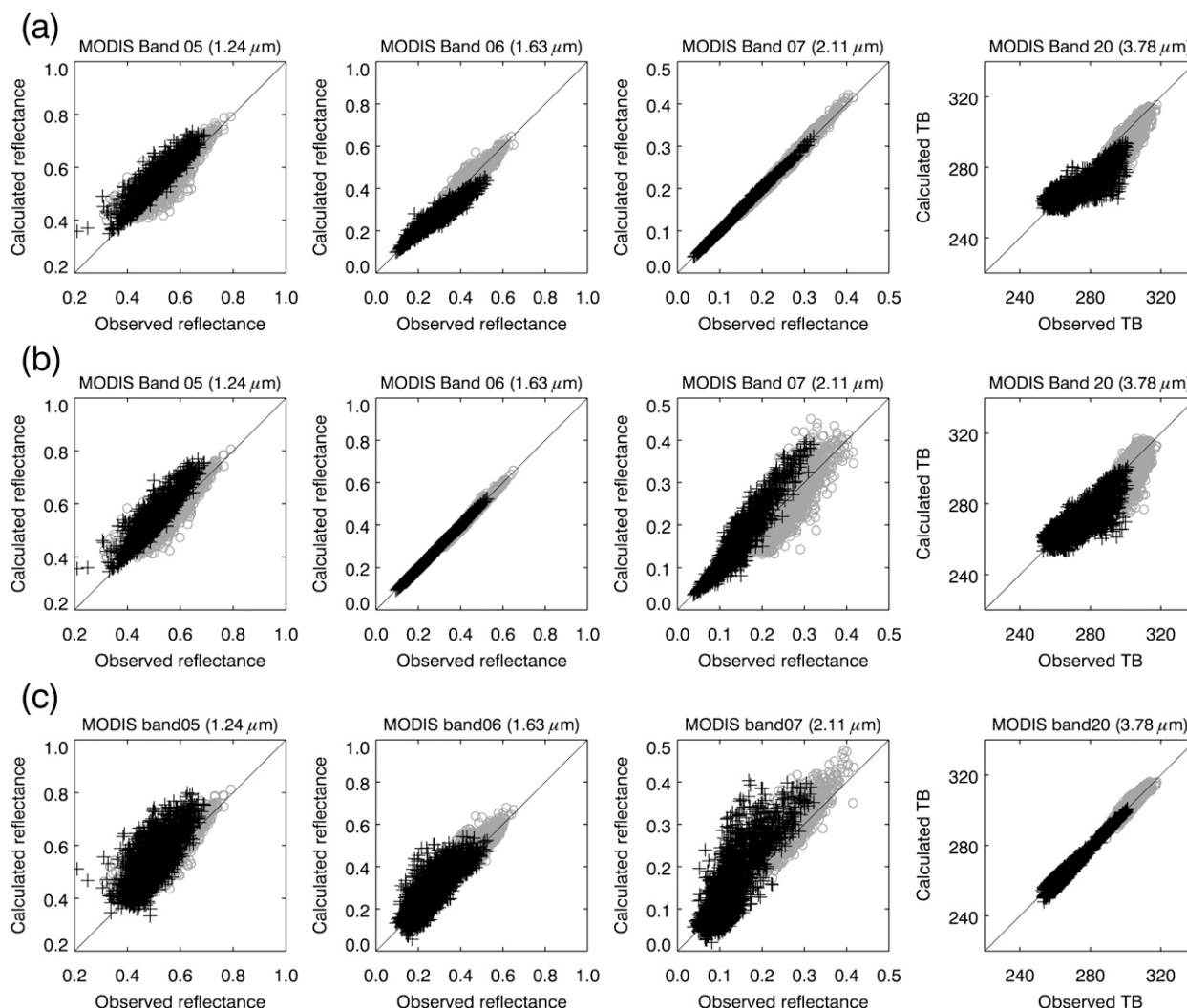


FIG. A1. Scatterplots of simulated vs observed reflectances (or TBs) at four SWIR/NIR bands for ice (black crosses) and water (gray circles) cloud pixels. Effective radii retrieved from (a) band 7 ( $2.11\ \mu\text{m}$ ), (b) band 6 ( $1.63\ \mu\text{m}$ ), and (c) band 20 ( $3.78\ \mu\text{m}$ ) are used as inputs to the RTM.

TABLE B1. The ratio of reflectances (or TBs) for CTH = 5 km to the values for CTH = 12 km with  $\Delta Z_c = 1$  km, that is,  $\alpha(Z_c = 5 \text{ km})$ , whereas water vapor profile and COT are varying.

Water vapor profile	$\rho_{\text{H}_2\text{O}}(z)$				$\rho_{\text{H}_2\text{O}}(z) \times 2/3$				$\rho_{\text{H}_2\text{O}}(z) \times 1/3$				
	COT	10	20	30	40	10	20	30	40	10	20	30	40
band 1 (0.646 $\mu\text{m}$ )		0.994	0.993	0.993	0.993	0.995	0.994	0.994	0.994	0.996	0.995	0.995	0.995
band 2 (0.857 $\mu\text{m}$ )		0.998	0.998	0.998	0.999	0.999	0.999	0.999	0.999	0.999	0.999	0.999	1.000
band 3 (0.466 $\mu\text{m}$ )		1.003	1.001	1.001	1.001	1.003	1.002	1.001	1.001	1.003	1.002	1.001	1.001
band 4 (0.554 $\mu\text{m}$ )		0.997	0.996	0.996	0.996	0.998	0.997	0.996	0.996	0.998	0.997	0.996	0.996
band 5 (1.24 $\mu\text{m}$ )		0.992	0.992	0.992	0.992	0.992	0.992	0.992	0.992	0.992	0.992	0.992	0.992
band 6 (1.63 $\mu\text{m}$ )		0.989	0.990	0.990	0.990	0.989	0.990	0.990	0.990	0.990	0.990	0.990	0.990
band 7 (2.11 $\mu\text{m}$ )		0.987	0.988	0.989	0.989	0.990	0.991	0.991	0.991	0.993	0.993	0.993	0.995
band 17 (0.904 $\mu\text{m}$ )		0.899	0.901	0.902	0.904	0.922	0.923	0.924	0.926	0.951	0.952	0.953	0.954
band 18 (0.936 $\mu\text{m}$ )		0.601	0.609	0.615	0.620	0.665	0.671	0.677	0.682	0.758	0.763	0.767	0.770
band 19 (0.936 $\mu\text{m}$ )		0.839	0.842	0.845	0.847	0.871	0.872	0.874	0.876	0.913	0.914	0.916	0.917
band 26 (1.38 $\mu\text{m}$ )		0.098	0.109	0.119	0.127	0.147	0.160	0.171	0.180	0.249	0.264	0.279	0.291
band 20 (3.78 $\mu\text{m}$ )		1.069	1.071	1.071	1.070	1.070	1.071	1.071	1.071	1.070	1.072	1.072	1.071
band 29 (8.56 $\mu\text{m}$ )		1.218	1.225	1.226	2.226	1.219	1.225	1.226	1.227	1.219	1.226	1.227	1.227
band 31 (11 $\mu\text{m}$ )		1.223	1.228	1.229	1.230	1.223	1.228	1.229	1.230	1.223	1.228	1.229	1.230
band 32 (12 $\mu\text{m}$ )		1.225	1.229	1.230	1.231	1.225	1.229	1.230	1.231	1.225	1.229	1.230	1.231

SWIR/NIR bands (1.24, 1.63, 2.11, and 3.78  $\mu\text{m}$ ). This may be a result of the effective radius retrieved from the 2.11- $\mu\text{m}$  band measurement being used for the radiance simulations. Thus, we expect likewise that other SWIR/NIR band can also be simulated with a similar accuracy if the effective radius derived from a given band is used for the same band's simulation. To test the sensitivity of radiance simulations to the effective radius inferred from different bands, SWIR/NIR reflectances are simulated with effective radii from band 6 (1.63  $\mu\text{m}$ ) and from band 20 (3.78  $\mu\text{m}$ ). Their respective results are given in Figs. A1b and A1c. For comparison, simulated results using 2.11- $\mu\text{m}$ -derived effective radii are also presented in Fig. A1a. As expected, simulated reflectances at 1.63  $\mu\text{m}$  show the best agreement with the observed values when 1.63- $\mu\text{m}$ -retrieved effective radii are used as RTM inputs, whereas other bands show more scattered patterns as the result of the inhomogeneous vertical distribution of particle sizes. In particular, band 7 (2.11  $\mu\text{m}$ ) shows increased scattered patterns. On the other hand, 1.24- and 3.78- $\mu\text{m}$  bands appear to be less sensitive to the bands chosen for the effective radius retrieval.

In Fig. A1c, when 3.78- $\mu\text{m}$ -retrieved effective radii are used for the simulation, the 3.78- $\mu\text{m}$  band shows the best agreement between simulated and observed values. However, the scattered patterns found in other channels seem to be more serious in comparison to patterns found in Figs. A1a and A1b, probably because the 3.78- $\mu\text{m}$  band is not only affected by cloud particle radius but also by the representative cloud depth. Therefore, it is concluded that 3.78- $\mu\text{m}$ -retrieved effective radii may have more uncertainties in comparison with the 1.63- or 2.11- $\mu\text{m}$ -retrieved effective radii.

## APPENDIX B

### Influences of CTH, Geometrical Depth, and the Vertical Distribution of Hydrometeors on TOA Radiances

The sensitivity of TOA radiances to the assigned CTH, cloud geometrical depth ( $\Delta Z_c$ ), and vertical distribution of hydrometeors is examined from radiative transfer simulations. The effect of water vapor variations on TOA radiances is studied with three sets of water vapor profiles: (i) January 2007 mean profile [ $\rho_{\text{H}_2\text{O}}(z)$ ]; (ii)  $\rho_{\text{H}_2\text{O}}(z) \times 1/3$ ; and (iii)  $\rho_{\text{H}_2\text{O}}(z) \times 2/3$ . Four different COT values—10, 20, 30, and 40—are used for the sensitivity test. Thus, there are 12 combinations, depending on the chosen water vapor profile and COT.

For the given water vapor profile and COT, influences of the CTH are examined by assuming the CTH to be from 5 to 12 km. For all the cases, a fixed 1-km cloud depth ( $\Delta Z_c = 1$  km) is used. Presenting the CTH sensitivity results, reflectances from the given CTH at 15 bands are normalized using reflectances (or TBs) from CTH = 12 km, that is,

$$\alpha(Z_c) = \frac{\text{simulated reflectance (TB)}_{z_c}}{\text{simulated reflectance (TB)}_{z_c=12 \text{ km}}}, \quad (\text{B1})$$

where  $\alpha(Z_c)$  is the normalized reflectance (or TB) for a given CTH ( $Z_c$ ). The values of  $\alpha(Z_c = 5 \text{ km})$  in Eq. (B1) are summarized in Table B1. It is shown that SW bands from 0.46 to 0.86  $\mu\text{m}$  (bands 1–4) and NIR bands (bands 5–7) are not very sensitive to the cloud height because of the near-unity value ( $\sim 1$ ), regardless of the chosen

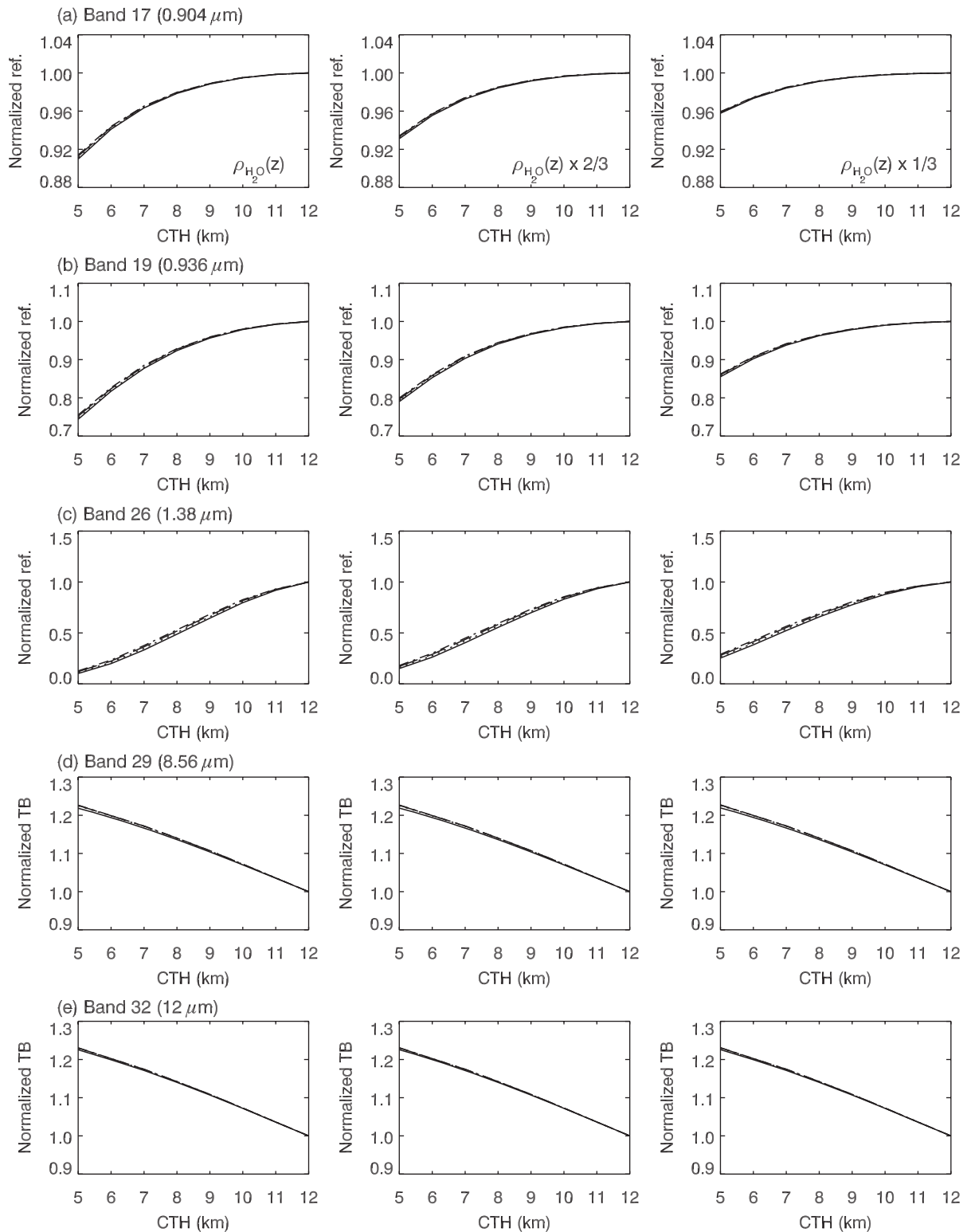


FIG. B1. Effect of CTH changes on normalized reflectances (or TBs) at (a) band 17 ( $0.904 \mu\text{m}$ ), (b) band 19 ( $0.936 \mu\text{m}$ ), (c) band 26 ( $1.38 \mu\text{m}$ ), (d) band 29 ( $8.56 \mu\text{m}$ ), and (e) band 32 ( $12 \mu\text{m}$ ) when  $\Delta Z_c = 1 \text{ km}$ . Three columns represent three different water vapor profiles given in (a). Simulated reflectances (or TBs) are normalized by the value for  $\text{CTH} = 12 \text{ km}$ . Four COT values (10, 20, 30, and 40) are delineated with different lines (solid, dotted, dashed, and dashed-dotted, respectively).



TABLE B2. The ratio of reflectances (or TBs) for  $\Delta Z_c = 7$  km to the values for  $\Delta Z_c = 1$  km with CTH = 12 km, that is,  $\beta(\Delta Z_c = 7 \text{ km})$ , whereas water vapor profile and COT are varying.

Water vapor profile	$\rho_{\text{H}_2\text{O}}(z)$				$\rho_{\text{H}_2\text{O}}(z) \times 2/3$				$\rho_{\text{H}_2\text{O}}(z) \times 1/3$				
	COT	10	20	30	40	10	20	30	40	10	20	30	40
band 1 (0.646 $\mu\text{m}$ )		0.998	0.997	0.997	0.997	0.998	0.997	0.997	0.998	0.998	0.998	0.998	0.998
band 2 (0.857 $\mu\text{m}$ )		1.000	1.000	1.000	1.000	1.000	1.000	1.000	1.000	1.000	1.000	1.000	1.000
band 3 (0.466 $\mu\text{m}$ )		1.000	1.000	1.000	1.000	1.000	1.000	1.000	1.000	1.000	1.000	1.000	1.000
band 4 (0.554 $\mu\text{m}$ )		0.999	0.998	0.998	0.998	0.999	0.998	0.998	0.998	0.999	0.998	0.998	0.998
band 5 (1.24 $\mu\text{m}$ )		0.996	0.996	0.997	0.997	0.996	0.996	0.997	0.997	0.996	0.996	0.997	0.997
band 6 (1.63 $\mu\text{m}$ )		0.996	0.998	0.998	0.999	0.997	0.998	0.998	0.999	0.997	0.998	0.998	0.999
band 7 (2.11 $\mu\text{m}$ )		0.998	1.000	1.000	1.000	0.999	1.000	1.000	1.000	0.999	1.000	1.000	1.000
band 17 (0.904 $\mu\text{m}$ )		0.972	0.977	0.981	0.983	0.979	0.983	0.986	0.988	0.987	0.989	0.991	0.992
band 18 (0.936 $\mu\text{m}$ )		0.872	0.898	0.914	0.925	0.895	0.916	0.930	0.930	0.927	0.942	0.951	0.958
band 19 (0.936 $\mu\text{m}$ )		0.953	0.962	0.968	0.972	0.963	0.970	0.975	0.978	0.976	0.980	0.984	0.986
band 26 (1.38 $\mu\text{m}$ )		0.621	0.714	0.782	0.831	0.660	0.746	0.809	0.853	0.726	0.799	0.851	0.887
band 20 (3.78 $\mu\text{m}$ )		1.009	1.003	1.002	1.002	1.009	1.003	1.002	1.002	1.009	1.003	1.002	1.002
band 29 (8.56 $\mu\text{m}$ )		1.044	1.022	1.015	1.011	1.044	1.022	1.015	1.011	1.044	1.022	1.015	1.011
band 31 (11 $\mu\text{m}$ )		1.041	1.021	1.014	1.010	1.041	1.021	1.014	1.010	1.041	1.021	1.014	1.010
band 32 (12 $\mu\text{m}$ )		1.039	0.020	1.013	1.010	1.039	0.020	1.013	1.010	1.039	0.020	1.013	1.010

water vapor profile and COT. However, water vapor bands, such as band 17 (0.904  $\mu\text{m}$ ), band 18 (0.936  $\mu\text{m}$ ), band 19 (0.936  $\mu\text{m}$ ), and band 26 (1.38  $\mu\text{m}$ ) show  $\alpha(Z_c = 5 \text{ km}) < 1$ , indicating that reflectances in those bands decrease when the CTH is moved from 12 to 5 km. This is expected because the column amount of water vapor above the cloud top increases as the CTH decreases from 12 to 5 km, inducing larger absorption in the water vapor bands. In addition, it is found that the reduction of water vapor band reflectances caused by changing CTH from 12 to 5 km becomes smaller for the case of  $\rho_{\text{H}_2\text{O}}(z) \times 1/3$  compared to the case of  $\rho_{\text{H}_2\text{O}}(z)$  [e.g., when COT = 10,  $\alpha(Z_c = 5 \text{ km})$  values of band 17 for  $\rho_{\text{H}_2\text{O}}(z)$  and  $\rho_{\text{H}_2\text{O}}(z) \times 1/3$  are 0.899 and 0.951, respectively]. For window bands—such as bands 20, 29, 31, and 32 (3.78, 8.56, 11, and 12  $\mu\text{m}$ , respectively)— $\alpha(Z_c = 5 \text{ km}) > 1$ , reflecting the influences of the warmer CTT of the lower cloud height (5 km) compared to the higher cloud top (12 km).

Figure B1 represents the values of  $\alpha$  for  $Z_c = 5$ –12 km in Eq. (B1) with varying water vapor profile and COT. Water vapor profiles are given in three columns, and four COT variations are given in each diagram of Fig. B1. Only water vapor bands (bands 17, 19, and 26) and window bands (bands 29 and 32) are displayed in Fig. B1 because those bands are highly sensitive to the CTH, whereas SW, SWIR, and NIR bands are less sensitive, as demonstrated in Table B1. Moreover, band 18 (0.936  $\mu\text{m}$ ) and band 31 (11  $\mu\text{m}$ ) are not displayed because those bands show similar behaviors to those shown in band 19 and band 32, respectively. It is found that the use of a mean water vapor profile [ $\rho_{\text{H}_2\text{O}}(z)$ ] results in 0.904-, 0.936-, and 1.38- $\mu\text{m}$  reflectances monotonically decreased by 10%, 15%, and 80%, respectively, when

CTH decreases from 12 to 5 km. In contrast, about a 20% increase is noted for 8.56 and 12  $\mu\text{m}$ . The decreasing and increasing trends with the CTH change are not greatly affected by the COT variation (from COT = 10 to COT = 40).

Another sensitivity test is performed to examine the influences of cloud geometrical depth ( $\Delta Z_c$ ) variation on the TOA radiances. In this test, the CTH is fixed at 12 km and the cloud-base height is (CTH –  $\Delta Z_c$ ) for the given cloud geometrical depth. For the given water vapor profile and COT, reflectances (or TB) are calculated with  $\Delta Z_c$  varying from 1 to 7 km, and the results are presented with the ratios of reflectances with the given  $\Delta Z_c$  to the values with  $\Delta Z_c = 1$  km, which is defined as follows:

$$\beta(\Delta Z_c) = \frac{\text{simulated reflectance (or TB)}_{\Delta Z_c}}{\text{simulated reflectance (or TB)}_{\Delta Z_c = 1 \text{ km}}}, \quad (\text{B2})$$

where  $\beta(\Delta Z_c)$  is the normalized reflectance (or TB) for a given  $\Delta Z_c$ . The values of  $\beta(\Delta Z_c = 7 \text{ km})$  in Eq. (B2) are presented in Table B2. Bands 1–7 show near-unity values ( $\sim 1$ ), indicating that the dependence of those bands on  $\Delta Z_c$  is insignificant. In contrast, water vapor bands (bands 17–19, and 26) show a smaller sensitivity ratio, implying that the water vapor absorption within the cloud layer has been increased as a result of the increased geometrical depth from 1 to 7 km. Similar to the CTH sensitivity results given in Table B1, the dependence of reflectance on  $\Delta Z_c$  becomes smaller when the atmospheric column gets drier—compare the results in the first column [ $\rho_{\text{H}_2\text{O}}(z)$ ] with those in the third column [ $\rho_{\text{H}_2\text{O}}(z) \times 1/3$ ].

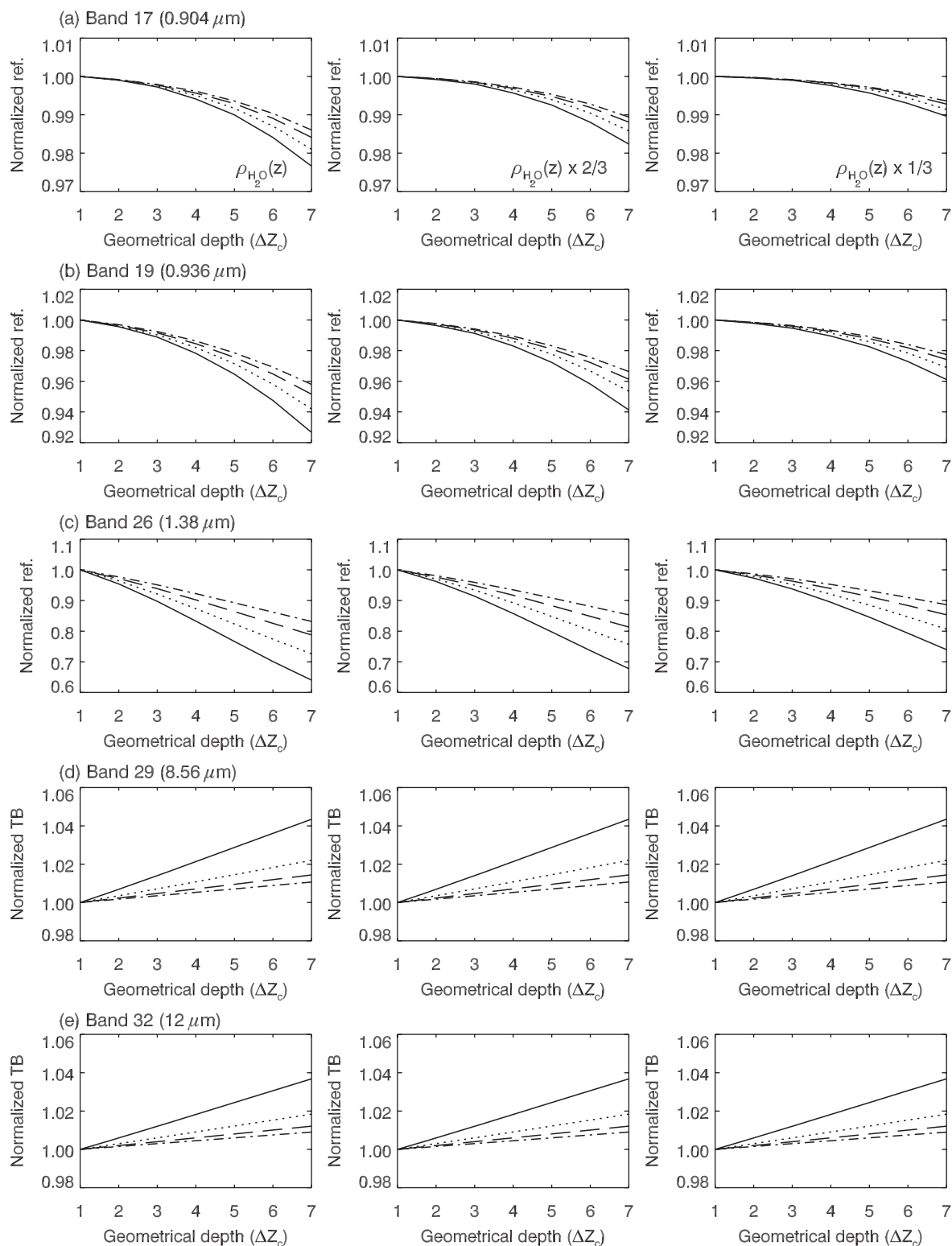


FIG. B2. As in Fig. B1 but CTH = 12 km (and thus  $\Delta Z_c$  from 1 to 7 km). Calculated reflectances (or TBs) are normalized values with  $\Delta Z_c = 1$  km.

TABLE B3. The ratio of reflectances (or TBs) for  $F_{\text{upper}} = 0.1$  to the values for  $F_{\text{upper}} = 1$ , i.e.,  $\gamma(F_{\text{upper}} = 0.1)$ , where  $F_{\text{upper}}$  is defined as the ratio of upper-layer COT to total COT. Two cloud layers are assumed to be located at 1–2 km and 11–12 km, respectively.

Water vapor profile COT	$\rho_{\text{H}_2\text{O}}(z)$				$\rho_{\text{H}_2\text{O}}(z) \times 2/3$				$\rho_{\text{H}_2\text{O}}(z) \times 1/3$			
	10	20	30	40	10	20	30	40	10	20	30	40
Band 1 (0.646 $\mu\text{m}$ )	0.979	0.976	0.975	0.974	0.983	0.980	0.979	0.978	0.987	0.985	0.984	0.983
Band 2 (0.857 $\mu\text{m}$ )	0.992	0.991	0.990	0.990	0.995	0.994	0.993	0.993	0.997	0.997	0.997	0.996
Band 3 (0.466 $\mu\text{m}$ )	1.002	1.000	0.999	0.999	1.002	1.000	0.999	0.999	1.002	1.000	1.000	0.999
Band 4 (0.554 $\mu\text{m}$ )	0.992	0.990	0.988	0.987	0.992	0.990	0.989	0.988	0.993	0.991	0.989	0.989
Band 5 (1.24 $\mu\text{m}$ )	0.989	0.988	0.988	0.988	0.992	0.992	0.991	0.991	0.995	0.995	0.995	0.995
Band 6 (1.63 $\mu\text{m}$ )	0.978	0.980	0.984	0.987	0.979	0.981	0.985	0.987	0.981	0.983	0.986	0.988
Band 7 (2.11 $\mu\text{m}$ )	0.959	0.969	0.977	0.984	0.968	0.976	0.982	0.987	0.979	0.984	0.988	0.991
Band 17 (0.904 $\mu\text{m}$ )	0.762	0.762	0.767	0.774	0.804	0.803	0.806	0.812	0.865	0.863	0.864	0.867
Band 18 (0.936 $\mu\text{m}$ )	0.314	0.342	0.376	0.411	0.387	0.407	0.435	0.464	0.514	0.525	0.543	0.563
Band 19 (0.936 $\mu\text{m}$ )	0.469	0.485	0.507	0.531	0.537	0.548	0.565	0.585	0.650	0.654	0.664	0.677
Band 26 (1.38 $\mu\text{m}$ )	0.124	0.188	0.258	0.326	0.125	0.189	0.259	0.328	0.136	0.199	0.268	0.337
Band 20 (3.78 $\mu\text{m}$ )	1.065	1.051	1.037	1.027	1.067	1.052	1.038	1.027	1.068	1.053	1.038	1.027
Band 29 (8.56 $\mu\text{m}$ )	1.189	1.135	1.092	1.061	1.190	1.136	1.093	1.062	1.192	1.138	1.094	1.063
Band 31 (11 $\mu\text{m}$ )	1.180	1.120	1.077	1.049	1.181	1.121	1.078	1.050	1.182	1.121	1.078	1.050
Band 32 (12 $\mu\text{m}$ )	1.173	1.109	1.067	1.041	1.174	1.109	1.067	1.041	1.175	1.110	1.067	1.041

The window bands (bands 20, 29, 31, and 32) show  $\beta(\Delta Z_c = 7 \text{ km}) > 1$ , implying that TBs at window bands have increased as a result of the increased mean temperature corresponding to the increased cloud depth. It is noted that the sensitivity tends to be smaller if COT increases, even though the value itself is larger than 1. This occurs because for large COT, clouds can be regarded as a blackbody and the signals emitted are largely determined by cloud-top temperature in the upper part of the cloud despite increased  $\Delta Z_c$ . However, for optically thin clouds,  $\Delta Z_c$  influences cannot be ignored because of the radiance transmitted through the cloud layer.

Figure B2 shows the values of  $\beta$  for  $\Delta Z_c = 1$ –7 km in Eq. (B2), whereas the water vapor profile and COT vary. As in Fig. B1, three water vapor profiles and four COT values are used for the calculation of five bands (bands 17, 19, 26, 29, and 32). The use of a mean water vapor profile demonstrates that 0.904-, 0.936-, and 1.38- $\mu\text{m}$  reflectances decrease by 3%, 5%, and 40%, respectively, when  $\Delta Z_c$  increases from 1 to 7 km. In contrast, an increase of about 4% is shown for 8.56 and 12  $\mu\text{m}$ . The deviations in the water vapor and window bands with  $\Delta Z_c$  variations (Fig. B2) are smaller compared to those due to CTH variations (Fig. B1), indicating the relatively larger effect of CTH rather than  $\Delta Z_c$  on water vapor and window bands.

In this study, we assumed that the contribution of any cloud layer to the total optical thickness is proportional to its geometrical depth. However, considering that the vertical distribution of hydrometeors within any cloud layer may not be homogenous, it is interesting to examine how a vertically varying optical contribution influences the TOA radiance simulations. To examine such influences, we performed a sensitivity test by as-

suming various ratios of COT contributions from two cloud layers, which are assumed to be located at 1–2 and 11–12 km, respectively. Here  $F_{\text{upper}}$  is defined as a COT fraction to the total COT by upper-level cloud, and 11 values of  $F_{\text{upper}}$  are considered to be from 0 to 1 with an interval of 0.1. Therefore,  $F_{\text{upper}} = 1$  (or 0) means that the COT is only from the upper (or lower) cloud layer. For a given  $F_{\text{upper}}$ , results are presented by normalizing the simulated reflectances (or TBs) with values from  $F_{\text{upper}} = 1$ , that is,

$$\gamma(F_{\text{upper}}) = \frac{\text{simulated reflectance (or TB)}_{F_{\text{upper}}}}{\text{simulated reflectance (or TB)}_{F_{\text{upper}}=1}}, \quad (\text{B3})$$

where  $\gamma(F_{\text{upper}})$  is the normalized reflectance (or TB) for a given  $F_{\text{upper}}$ . The values of  $\gamma(F_{\text{upper}} = 0.1)$  are presented in Table B3 to examine MODIS bands sensitive to the rationed COT contribution. It is noted that bands 1–7 show smaller deviations from 1 compared to other water vapor or window bands, which means that those bands are less sensitive to the COT rationing. Water vapor bands (bands 17–19, and 26) show  $\gamma(F_{\text{upper}} = 0.1) < 1$ , implying that water vapor absorption above and within the lower cloud layer has been increased as a result of the change of  $F_{\text{upper}}$  from 1 to 0.1 (i.e., an increased weighting to the lower cloud). The window bands (bands 20, 29, 31, and 32) show  $\gamma(F_{\text{upper}} = 0.1) > 1$ , implying that TBs at window bands are increased as a result of the shift of the mean temperature to the lower cloud layer.

Normalized reflectances and TBs ( $\gamma$ ) for various values of  $F_{\text{upper}}$  are given in Fig. B3 but are the same as in the previous two sensitivity tests; only water vapor

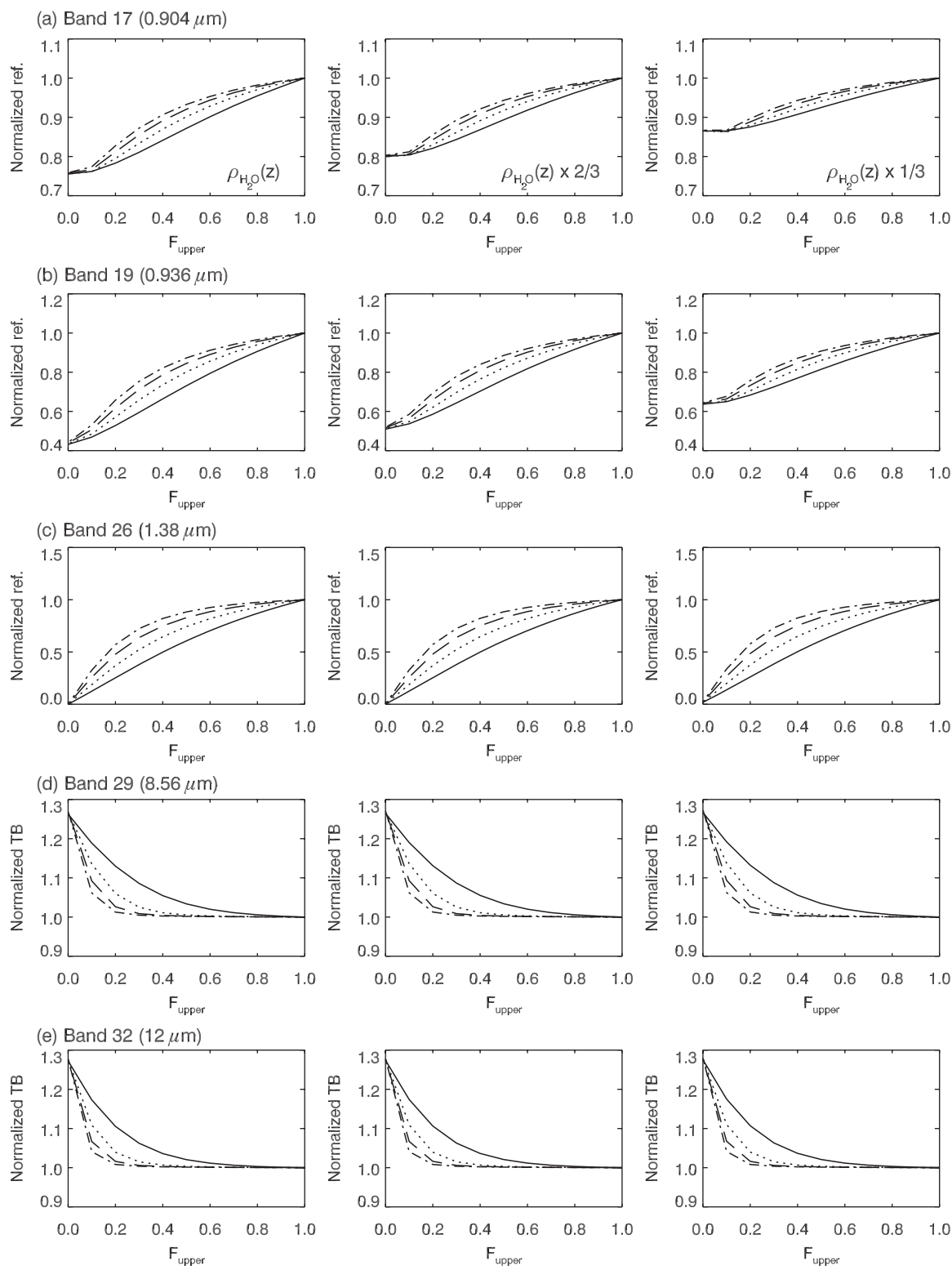


FIG. B3. As in Fig. B1 but for the COT fraction of upper-cloud layer ( $F_{\text{upper}}$ ) instead of CTH. Upper and lower clouds are assumed to be located at  $1 \sim 2 \text{ km}$  and  $11 \sim 12 \text{ km}$ , respectively. Simulated reflectances (or TBs) are normalized by the values when  $F_{\text{upper}} = 1$ .



(bands 17, 19, and 26) and IR window bands (bands 29 and 32) are displayed. Because a large portion of COT transitions from lower cloud to the upper cloud—that is,  $F_{\text{upper}}$  increases—water vapor band reflectances increase as a result of a reduction of water vapor absorption. In contrast, TBs at window bands decrease with  $F_{\text{upper}}$  with the reduced cloud mean temperature. For COT = 10 (solid line in Fig. B3), a decreasing trend of IR TBs vanishes when  $F_{\text{upper}}$  exceeds about 0.7 because the upper cloud starts to emit nearly as a black-body regardless of the existence of lower cloud layer. In summary, these results suggest that caution must be exercised when satellite-derived COT information is directly interpreted without considering the vertical inhomogeneity of cloud hydrometeors.

## REFERENCES

- Ackerman, S. A., and G. L. Stephens, 1987: The absorption of solar radiation by cloud droplets: An application of anomalous diffraction theory. *J. Atmos. Sci.*, **44**, 1574–1588.
- Aumann, H. H., and Coauthors, 2003: AIRS/AMSU/HSB on the Aqua mission: Design, science objectives, data products, and processing systems. *IEEE Trans. Geosci. Remote Sens.*, **41**, 253–264.
- Barkstrom, B. R., and G. L. Smith, 1986: The Earth Radiation Budget Experiment: Science and implementation. *Rev. Geophys.*, **24**, 379–390.
- Barnes, W. L., T. S. Pagano, and V. V. Salomonson, 1998: Pre-launch characteristics of the Moderate Resolution Imaging Spectroradiometer (MODIS) on EOS-AM1. *IEEE Trans. Geosci. Remote Sens.*, **36**, 1088–1100.
- Baum, B. A., and B. A. Wielicki, 1994: Cirrus cloud retrieval using infrared sounding data: Multilevel cloud errors. *J. Appl. Meteor.*, **33**, 107–117.
- , A. J. Heymsfield, P. Yang, and S. T. Bedka, 2005a: Bulk scattering models for the remote sensing of ice clouds. Part I: Microphysical data and models. *J. Appl. Meteor.*, **44**, 1885–1895.
- , P. Yang, A. J. Heymsfield, S. Platnick, M. D. King, Y.-X. Hu, and S. T. Bedka, 2005b: Bulk scattering models for the remote sensing of ice clouds. Part II: Narrowband models. *J. Appl. Meteor.*, **44**, 1896–1911.
- Fishbein, E., and Coauthors, 2007: AIRS Version 5 Release Level 2 Standard Product QuickStart. [Available online at [http://disc.sci.gsfc.nasa.gov/AIRS/documentation/v5\\_docs/AIRS\\_V5\\_Release\\_User\\_Docs/V5\\_L2\\_Standard\\_Product\\_QuickStart.pdf](http://disc.sci.gsfc.nasa.gov/AIRS/documentation/v5_docs/AIRS_V5_Release_User_Docs/V5_L2_Standard_Product_QuickStart.pdf).]
- Frey, R. A., S. A. Ackerman, Y. Liu, K. I. Strabala, H. Zhang, J. R. Key, and X. Wang, 2008: Cloud detection with MODIS. Part I: Improvements in the MODIS cloud mask for collection 5. *J. Atmos. Oceanic Technol.*, **25**, 1057–1072.
- Hartmann, D. L., and D. Doelling, 1991: On the net radiative effectiveness of clouds. *J. Geophys. Res.*, **96**, 869–891.
- Heymsfield, A. J., and J. Iaquinta, 2000: Cirrus crystal terminal velocities. *J. Atmos. Sci.*, **57**, 916–938.
- , A. Bansemer, P. R. Field, S. L. Durden, J. Stith, J. E. Dye, W. Hall, and T. Grainger, 2002: Observations and parameterizations of particle size distributions in deep tropical cirrus and stratiform precipitating clouds: Results from in situ observations in TRMM field campaigns. *J. Atmos. Sci.*, **59**, 3457–3491.
- Hong, G., P. Yang, H.-L. Huang, B. A. Baum, Y. X. Hu, and S. Platnick, 2007: The sensitivity of ice cloud optical and microphysical passive satellite retrievals to cloud geometrical thickness. *IEEE Trans. Geosci. Remote Sens.*, **45**, 1315–1323.
- Hu, Y. X., B. Wielicki, B. Lin, G. Gibson, S.-C. Tsay, K. Stamnes, and T. Wong, 2000:  $\delta$ -Fit: A fast and accurate treatment of particle scattering phase functions with weighted singular-value decomposition least-squares fitting. *J. Quant. Spectrosc. Radiat. Transfer*, **65**, 681–690.
- Kahn, B. H., E. Fishbein, S. L. Nasiri, A. Eldering, E. J. Fetzer, M. J. Garay, and S.-Y. Lee, 2007: The radiative consistency of Atmospheric Infrared Sounder and Moderate Resolution Imaging Spectroradiometer cloud retrievals. *J. Geophys. Res.*, **112**, D09201, doi:10.1029/2006JD007486.
- , and Coauthors, 2008: Cloud type comparisons of AIRS, CloudSat, and CALIPSO cloud height and amount. *Atmos. Chem. Phys.*, **8**, 1231–1248.
- Kandel, R., and Coauthors, 1998: The ScaRaB Earth radiation budget dataset. *Bull. Amer. Meteor. Soc.*, **79**, 765–783.
- King, M. D., 1983: Number of terms required in the Fourier expansion of the reflection function for optically thick atmospheres. *J. Quant. Spectrosc. Radiat. Transfer*, **30**, 143–161.
- , S.-C. Tsay, S. Platnick, M. Wang, and K.-N. Liou, 1997: Cloud retrieval algorithms for MODIS: Optical thickness, effective particle radius, and thermodynamic phase. MODIS Algorithm Theoretical Basis Document ATBD-MOD-05, 83 pp.
- , S. Platnick, P. A. Hubanks, G. T. Arnold, E. G. Moody, G. Wind, and B. Wind, 2006: Collection 005 change summary for the MODIS cloud optical property (06\_OD) algorithm. [Available online at [http://modis-atmos.gsfc.nasa.gov/C005\\_Changes/C005\\_CloudOpticalProperties\\_ver311.pdf](http://modis-atmos.gsfc.nasa.gov/C005_Changes/C005_CloudOpticalProperties_ver311.pdf).]
- Kratz, D. P., 1995: The correlated  $k$ -distribution technique as applied to the AVHRR channels. *J. Quant. Spectrosc. Radiat. Transfer*, **53**, 501–517.
- , and F. G. Rose, 1999: Accounting for molecular absorption within the spectral range of the CERES window channel. *J. Quant. Spectrosc. Radiat. Transfer*, **61**, 83–95.
- Liou, K. N., 2002: *An Introduction to Atmospheric Radiation*. 2nd ed. Academic Press, 577 pp.
- Mace, G. G., R. Marchand, Q. Zhang, and G. Stephens, 2007: Global hydrometeor occurrence as observed by CloudSat: Initial observations from summer 2006. *Geophys. Res. Lett.*, **34**, L09808, doi:10.1029/2006GL029017.
- Menzel, W. P., R. A. Frey, B. A. Baum, and H. Zhang, 2006: Cloud top properties and cloud phase algorithm. MODIS Algorithm Theoretical Basis Document ATBD-MOD-04, 61 pp.
- , and Coauthors, 2008: MODIS global cloud-top pressure and amount estimation: Algorithm description and results. *J. Appl. Meteor. Climatol.*, **47**, 1175–1198.
- Nakajima, T., and M. Tanaka, 1988: Algorithm for radiative intensity calculations in moderate thick atmospheres using a truncation approximation. *J. Quant. Spectrosc. Radiat. Transfer*, **40**, 51–69.
- , and M. D. King, 1990: Determination of the optical thickness and effective particle radius of clouds from reflected solar radiation measurements. Part I: Theory. *J. Atmos. Sci.*, **47**, 1878–1893.
- Nasiri, S. L., and B. H. Kahn, 2008: Limitations of bispectral infrared cloud phase determination and potential for improvement. *J. Appl. Meteor. Climatol.*, **47**, 2895–2910.

- Palmer, K. F., and D. Williams, 1974: Optical properties of water in the near infrared. *J. Opt. Soc. Amer.*, **64**, 1107–1110.
- Platnick, S., 2001: A superposition technique for deriving photon scattering statistics in plane-parallel cloudy atmospheres. *J. Quant. Spectrosc. Radiat. Transfer*, **68**, 57–73.
- , M. D. King, S. A. Ackerman, W. P. Menzel, and R. O. Knuteson, 2003: The MODIS cloud products: Algorithms and examples from Terra. *IEEE Trans. Geosci. Remote Sens.*, **41**, 459–473.
- Ramanathan, V., R. D. Cess, E. F. Harrison, P. Minnis, B. R. Barkstrom, E. Ahmad, and D. Hartmann, 1989: Cloud-radiative forcing and climate: Results from the Earth Radiation Budget Experiment. *Science*, **243**, 57–63.
- Ricchiazzi, P., S. Yang, C. Gautier, and D. Sowle, 1998: SBDART: A research and teaching software tool for plane-parallel radiative transfer in the earth's atmosphere. *Bull. Amer. Meteor. Soc.*, **79**, 2101–2114.
- Roebeling, R. A., A. J. Feijt, and P. Stammes, 2006: Cloud property retrievals for climate monitoring: Implications of differences between Spinning Enhanced Visible and Infrared Imager (SEVIRI) on *METEOSAT-8* and Advanced Very High Resolution Radiometer (AVHRR) on *NOAA-17*. *J. Geophys. Res.*, **111**, D20210, doi:10.1029/2005JD006990.
- Salomonson, V. V., W. L. Barnes, P. W. Maymon, H. E. Montgomery, and H. Ostrow, 1989: MODIS: Advanced facility instrument for studies of the earth as a system. *IEEE Trans. Geosci. Remote Sens.*, **27**, 145–153.
- Smith, W. L., T. P. Charlock, R. Kahn, J. V. Martins, L. A. Remer, P. V. Hobbs, J. Redemann, and C. K. Rutledge, 2005: EOS *Terra* aerosol and radiative flux validation: An overview of the Chesapeake Lighthouse and Aircraft Measurements for Satellites (CLAMS) experiment. *J. Atmos. Sci.*, **62**, 903–918.
- Sohn, B. J., and E. A. Smith, 1992: The significance of cloud-radiative forcing to the general circulation on climate time scales—A satellite interpretation. *J. Atmos. Sci.*, **49**, 845–860.
- Solomon, S., D. Qin, M. Manning, M. Marquis, K. Averyt, M. M. B. Tignor, J. L. Miller Jr., and Z. Chen, 2007: *Climate Change 2007: The Physical Science Basis*. Cambridge University Press, 996 pp.
- Stamnes, K., S.-C. Tsay, W. J. Wiscombe, and K. Jayaweera, 1988: Numerically stable algorithm for discrete-ordinate-method radiative transfer in multiple scattering and emitting layered media. *Appl. Opt.*, **27**, 2502–2509.
- Stephens, G. L., and Coauthors, 2002: The *CloudSat* mission and the A-train: A new dimension of space-based observations of clouds and precipitation. *Bull. Amer. Meteor. Soc.*, **83**, 1771–1790.
- Susskind, J., C. D. Barnet, and J. M. Blaisdell, 2003: Retrieval of Atmospheric and surface parameters from AIRS/AMSU/HSB data in the presence of clouds. *IEEE Trans. Geosci. Remote Sens.*, **41**, 390–409.
- , J. Blaisdell, and P. Rosenkranz, 2007: AIRS/AMSU/HSB version 5 level 2 quality control and error estimation. E. T. Olsen, Ed., JPL Rep., 15 pp. [Available online at [http://disc.sci.gsfc.nasa.gov/giovanni/AIRS/documentation/documentation/v5\\_docs/AIRS\\_V5\\_Release\\_User\\_Docs/V5\\_L2\\_Quality\\_Control\\_and\\_Error\\_Estimation.pdf](http://disc.sci.gsfc.nasa.gov/giovanni/AIRS/documentation/documentation/v5_docs/AIRS_V5_Release_User_Docs/V5_L2_Quality_Control_and_Error_Estimation.pdf).]
- Tobin, D. C., H. E. Revercomb, C. C. Moeller, and T. S. Pagano, 2006: Use of Atmospheric Infrared Sounder high-spectral resolution spectra to assess the calibration of moderate resolution imaging spectroradiometer on EOS *Aqua*. *J. Geophys. Res.*, **111**, D09S05, doi:10.1029/2005JD006095.
- Turner, D. D., and Coauthors, 2004: The QME AERI LBLRTM: A closure experiment for downwelling high spectral resolution infrared radiance. *J. Atmos. Sci.*, **61**, 2657–2675.
- , and Coauthors, 2007: Thin liquid water clouds: Their importance and our challenge. *Bull. Amer. Meteor. Soc.*, **88**, 177–190.
- Weisz, E., J. Li, W. P. Menzel, A. K. Heidinger, B. H. Kahn, and C.-Y. Liu, 2007: Comparison of AIRS, MODIS, *CloudSat* and *CALIPSO* cloud top height retrievals. *Geophys. Res. Lett.*, **34**, L17811, doi:10.1029/2007GL030676.
- Wielicki, B. A., B. R. Barkstrom, E. F. Harrison, R. B. Lee III., G. L. Smith, and J. E. Cooper, 1996: Clouds and the Earth's Radiant Energy System (CERES): An Earth Observing System Experiment. *Bull. Amer. Meteor. Soc.*, **77**, 853–868.
- Winker, D. M., J. Pelon, and M. P. McCormick, 2003: The CALIPSO mission: Spaceborne lidar for observation of aerosols and clouds. *Lidar Remote Sensing for Industry and Environment Monitoring III*, U. N. Singh, T. Itabe, and Z. Liu, Eds., International Society for Optical Engineering (SPIE Proceedings, Vol. 4893), 1–11.
- Wiscombe, W. J., 1977: The Delta-*M* method: Rapid yet accurate radiative flux calculations for strongly asymmetric phase functions. *J. Atmos. Sci.*, **34**, 1408–1422.
- Xiong, X., and W. L. Barnes, 2003: Early on-orbit calibration results from *Aqua* MODIS. *Sensors, Systems, and Next-Generation Satellites VI*, H. Fujisada et al., Eds., International Society for Optical Engineering (SPIE Proceedings, Vol. 4881), 327–336.
- Yang, P., K. N. Liou, K. Wyser, and D. Mitchell, 2000: Parameterization of the scattering and absorption properties of individual ice crystals. *J. Geophys. Res.*, **105**, 4699–4718.
- , B. A. Baum, A. J. Heymsfield, Y. X. Hu, H.-L. Huang, S.-C. Tsay, and S. A. Ackerman, 2003: Single-scattering properties of droxtals. *J. Quant. Spectrosc. Radiat. Transfer*, **79–80**, 1159–1169.
- , H. Wei, H.-L. Huang, B. A. Baum, Y. X. Hu, G. W. Kattawar, M. I. Mishchenko, and Q. Fu, 2005: Scattering and absorption property database for nonspherical ice particles in the near-through far-infrared spectral region. *Appl. Opt.*, **44**, 5512–5523.
- , L. Zhang, G. Hong, S. L. Nasiri, B. A. Baum, H.-L. Huang, M. D. King, and S. Platnick, 2007: Differences between Collection 4 and 5 MODIS ice cloud optical/microphysical products and their impact on radiative forcing simulations. *IEEE Trans. Geosci. Remote Sens.*, **45**, 2886–2899.